



Full length article



# Grain boundary self- and Mn impurity diffusion in equiatomic CoCrFeNi multi-principal element alloy

Sandipan Sen<sup>a,b,\*</sup>, Marcel Glienke<sup>a</sup>, Bhawna Yadav<sup>c</sup>, Mayur Vaidya<sup>c</sup>, K. Gururaj<sup>d</sup>, K.G. Pradeep<sup>d</sup>, Lydia Daum<sup>a</sup>, Bengü Tas<sup>a</sup>, Lukasz Rogal<sup>e</sup>, Gerhard Wilde<sup>a</sup>, Sergiy V. Divinski<sup>a,\*\*</sup>

<sup>a</sup> Institute of Materials Physics, University of Münster, Wilhelm-Klemm-Str. 10, 48149 Münster, Germany

<sup>b</sup> Institute for Applied Materials (IAM-WK), Karlsruhe Institute of Technology (KIT), Engelbert-Arnold-Strasse 4, 76131 Karlsruhe, Germany

<sup>c</sup> Department of Materials Science and Metallurgical Engineering, Indian Institute of Technology Hyderabad, Kandi, Sangareddy, 502285, India

<sup>d</sup> Correlative Microscopy Lab, Department of Metallurgical and Materials Engineering, Indian Institute of Technology Madras, Chennai 600036, India

<sup>e</sup> Institute of Metallurgy and Materials Science, Polish Academy of Sciences, Reymonta 25 Str., 30-059 Krakow, Poland

## ARTICLE INFO

### Keywords:

Grain boundary diffusion  
High-entropy alloy  
Phase decomposition  
Segregation  
CoCrFeNi

## ABSTRACT

Grain boundary self-diffusion of Co, Cr and Fe and impurity diffusion of Mn are measured in a coarse-grained equiatomic CoCrFeNi multi-principal alloy. The tracer diffusivities are determined in a wide temperature range of 643 K to 1273 K, which encompasses both the C- and B-type kinetic regimes of grain boundary diffusion in polycrystalline materials after Harrison's classification. At higher temperatures ( $T > 800$  K), only one short-circuit (grain boundary) contribution is observed, while the existence of two distinct contributions is elucidated by thorough analysis of the penetration profiles corresponding to the C-type kinetic regime (643–703 K). The latter observations are explained in terms of a grain boundary phase decomposition after prolonged annealing below 700 K. The product of the segregation factor and the grain boundary width is found to be about 0.5 nm for all constituting elements. The grain boundary diffusion data indicate that Mn does not reveal a strong (if any) segregation in the equiatomic CoCrFeNi alloy.

## 1. Introduction

The last decade has seen an exponential increase in the exploration of high entropy alloys (HEAs). This new class of multi-component alloys, which combines elements in equiatomic or near equiatomic proportions, have garnered fundamental curiosity and technological interest of the scientific community [1,2]. The multi-principal element matrix of HEAs, maximizing the configurational entropy, was believed to be responsible for their exciting features and properties [2]. For example, a novel quasi-peritectic (CoCrFeNi)Zr HEA shows ultra-high strength [3], while enhanced strength–ductility synergy is exhibited by thermo-mechanically processed CoCrFeNi<sub>2.1</sub>Nb<sub>0.2</sub> [4]. The equiatomic BCC HEAs MoNbTaW and MoNbTaVW have shown exceptional strength retention up to 1900 K [5]. A nanostructured FeCrNiCoNb<sub>0.5</sub> HEA exhibits excellent corrosion resistance due to formation of an amorphous protective film [6], while good oxidation resistance is shown by an AlCuFeMn HEA [7]. Twin formation inducing high strength and ductility is exhibited by the equiatomic CoCrFeMnNi and CoCrFeNi HEAs [8]. Given the large compositional space available

with HEAs, a strategic assessment of HEAs and their most important features and properties seems required for facilitating accelerated design approaches (for example, see [9]). Thus, knowledge about the key factors controlling the structural and functional behaviour, environmental degradation, thermal stability and physical properties is essential to realize these multicomponent and multi-principal alloys for real-world applications.

It is generally recognized that a broad spectrum of properties and phenomena depends on the atomic transport within the crystalline lattice and/or along grain boundaries (GBs). Coble creep, recrystallization, grain growth, sintering, diffusion-induced GB migration and various discontinuous reactions are, e.g., controlled by GB diffusion [10]. In addition, diffusion measurements provide a highly sensitive tool for analysing atomic kinetics as well as delicate microstructural changes. Even the segregation behaviour of solutes in dilute and concentrated alloys can be probed by dedicated GB diffusion measurements [11–13]. Additionally, the knowledge of GB diffusivities is required, e.g., for the development of computational models for hot forming processes [14] or the investigation of creep behaviour in nanocrystalline materials [15].

\* Corresponding author at: Institute for Applied Materials (IAM-WK), Karlsruhe Institute of Technology (KIT), Engelbert-Arnold-Strasse 4, 76131 Karlsruhe, Germany.

\*\* Corresponding author.

E-mail addresses: [ssen@uni-muenster.de](mailto:ssen@uni-muenster.de) (S. Sen), [vaidyam@msme.iitb.ac.in](mailto:vaidyam@msme.iitb.ac.in) (M. Vaidya), [divin@uni-muenster.de](mailto:divin@uni-muenster.de) (S.V. Divinski).

<https://doi.org/10.1016/j.actamat.2023.119588>

Received 31 August 2023; Received in revised form 2 December 2023; Accepted 6 December 2023

Available online 7 December 2023

1359-6454/© 2023 The Authors. Published by Elsevier Ltd on behalf of Acta Materialia Inc. This is an open access article under the CC BY license (<http://creativecommons.org/licenses/by/4.0/>).

For high entropy alloys, four core effects were suggested and the concept of 'sluggish' diffusion as a consequence of the multi-principal element matrix presents one of these core effects that, according to the early predictions, distinguish HEA from conventional alloy behaviour [16]. However, recent *direct* measurements of the atomic transport rates using a radiotracer method [17–22], interdiffusion [23–25] and tracer-interdiffusion measurements [26] have revealed that sluggish diffusion in fact is not an inherent property of HEAs. Especially in non-FCC alloys, significant deviations from the anticipated behaviour are observed [27], as it was recently reported for BCC refractory Hf-TiZrNbTa and HfTiZrNbV alloys [28] and for the HCP AlHfTiScZr HEA system where an 'anti-sluggish' behaviour was indeed observed [22]. The experimental observations of the diffusion-controlled processes in HEAs have also suggested a non-sluggish atomic transport in these multi-principal alloys [29,30].

Up to now, the majority of diffusion studies on HEAs have been devoted to volume diffusion [17–20,22,31–33] across different crystal structures and different constituent elements, however only a few studies of GB diffusion in HEAs exist [34,35]. It is well established that grain boundaries offer high-diffusivity paths in metals and alloys [10]. A non-sluggish GB self-diffusion behaviour has been revealed for the constituent elements in CoCrFeMnNi relative to other FCC materials [34,35]. The same work demonstrated that GB diffusion can serve as a unique and non-local tool to probe the existence of phase decomposition in HEAs [35]. Two short-circuit contributions (relatively 'slow' and 'fast') to the GB self diffusion were observed at temperatures below about 700 K, which indicated the existence of two different types of general high-angle GBs in the investigated HEA at these temperatures. Atom probe tomography (APT) revealed the formation of Ni–Mn-rich and Cr-rich nano-precipitates at a fraction of the examined high-angle GBs [35]. Transmission electron microscopy [35] discovered the formation of a dislocation network at such GBs, which was proposed to be responsible for the 'fast' GB diffusion contribution. It should be emphasized that the relatively 'slow' contribution corresponds to diffusion rates similar to that of random high-angle GBs as they are present in well-annealed polycrystalline CoCrFeMnNi at elevated temperatures [35]. These diffusion pathways are conventionally the fastest short-circuit paths in well-annealed polycrystalline materials.

In contrast to these experimental results, a certain "sluggishness" of GB diffusion in the equiatomic FeNiCrCoCu high-entropy alloy has recently been observed by molecular dynamics studies [36]. The "sluggish" diffusion along a special  $\Sigma 5(210)[001]$  GB was explained by a "trapping effect" due to the compositional complexity in the HEA and the confined 2-D diffusion path [36]. However, Fan and Zhang [37] did not report similar observations for the diffusion along  $\Sigma 9$  and  $\Sigma 27$  GBs in equiatomic CoCrFeMnNi HEA. Furthermore, GB segregation in high-entropy alloys, mainly in equiatomic CoCrFeMnNi, was frequently addressed both theoretically [38–40] and experimentally [38,41]. As a result, a moderate Cr enrichment and a slight depletion of Mn below 1000 K in CoCrFeMnNi have been reported [38,41].

Based on the above, GB diffusion measurements on different multi-principal element alloys is required to provide the required insights into the phase stability and decomposition or precipitation occurring at the internal interfaces of these materials. GB diffusion of Ni was already measured in CoCrFeNi [34]. The present work explores GB self-diffusion of Co, Cr and Fe in the CoCrFeNi HEA by the radiotracer analysis utilizing their corresponding  $\gamma$ -isotopes. These analyses provide a complete characterization of self diffusion in the multi-component material, which is imperative, e.g., for a reliable treatment of diffusion-related phenomena with respect to heterogeneous precipitation [42]. Furthermore, GB diffusion of Mn as a solute element is measured for the first time and the corresponding segregation factor is evaluated.

## 2. Experimental details

### 2.1. Sample preparation

Solid metal pieces (99.9% purity) of Co, Cr, Fe and Ni were mixed in equiatomic proportion and melted together in a high-frequency induction melting furnace to produce CoCrFeNi HEA buttons. To homogenize the initial dendritic structure, the alloyed buttons were annealed at 1373 K for 50 h. Subsequently, 1 mm thick disc-shaped samples of 10 mm in diameter were cut for the diffusion experiments. The samples were mechanically polished and pre-annealed at the temperatures of the diffusion measurements for the intended diffusion annealing times. This procedure ensures equilibrium segregation (including that of residual impurities) at GBs and removes mechanical stresses induced into the samples during cutting, grinding or polishing.

The phase analysis of the pre-annealed alloys was performed using X-ray diffraction (XRD) with Cu- $K_{\alpha}$  radiation (measured with a step size of  $0.02^{\circ}$  and acquisition time of 2 s). Scanning electron microscopy (SEM, FEI Nova Nano-SEM 230) equipped with electron back-scatter diffraction (EBSD, TSL OIM software) and energy dispersive X-ray spectroscopy (EDS) was used to examine the microstructure of the samples.

Three-dimensional elemental distribution analysis with nearly atomic-scale resolution was performed using a local electrode atom probe (LEAP) (Cameca, 5000XR, USA). Site-specific APT tips inclusive of grain boundary regions were prepared using a dual-beam Focused ion beam (FIB) device (ThermoFisher scientific, Helios G4 UX) following the lift out procedure described in previous publications [43,44]. APT measurements were carried out in the laser pulsing mode with a laser pulse frequency of 250 kHz and 30 pJ pulse energy while the tips were maintained at a temperature of 60 K. Data reconstruction and analyses were performed using the IVAS 3.8.10 software provided by Cameca Inc.

### 2.2. Radiotracer measurements

The radioactive  $\gamma$ -isotopes of  $^{57}\text{Co}$  (122 keV, 271.7 days half-life),  $^{51}\text{Cr}$  (320 keV, 27.7 days half-life),  $^{59}\text{Fe}$  (1095 keV, 44.6 days half-life) and  $^{54}\text{Mn}$  (835 keV, 312.5 days half-life) were used for diffusion measurements. The highly diluted acidic solutions were sequentially applied to the polished surfaces of the pre-annealed samples. The total amount of the applied isotopes was small (several  $\mu\text{l}$ ) so that the chemical equilibrium of the samples remained unperturbed. Thus, the true tracer diffusion behaviour of the constituent elements was measured without inducing unwanted chemical diffusion and/or co-segregation effects.

The samples were sealed in quartz tubes under purified (5N) Ar atmosphere and annealed. For the annealing treatments, the furnace temperatures were controlled within  $\pm 1$  K using Ni/NiCr thermocouples (type K). After annealing, the samples were quenched in water.

The diameters of the samples were subsequently reduced by roughly 1 mm to avoid any effects of surface/ lateral diffusion. A high-precision grinding machine was used to measure the penetration profiles by parallel sectioning of the sample into thin slices with an accuracy of  $\pm 0.05$   $\mu\text{m}$ . The relative activity of each section was measured using a solid Ge  $\gamma$ -detector equipped with a 16K multi-channel energy discriminator (energy resolution of about 0.7 keV), which allowed a distinction of the activities of all four applied tracers simultaneously. Thus, the penetration profiles for all the tracers could be determined in a single experiment at a given temperature. The counting times of the detector were adjusted to keep the statistical uncertainties below 2%.

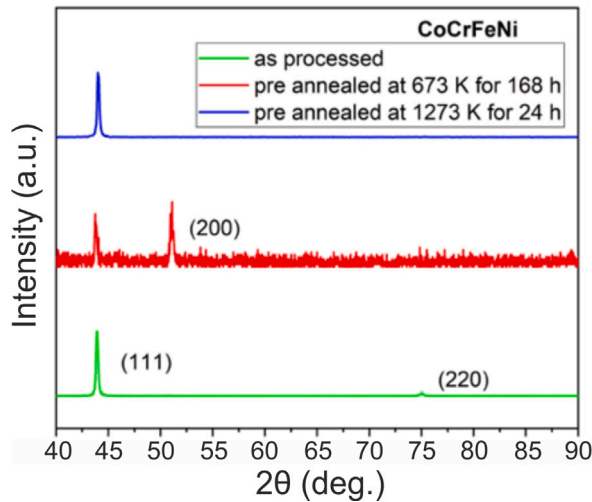


Fig. 1. XRD patterns of CoCrFeNi in as-processed and pre-annealed states. The recorded peaks are indexed.

### 3. Results

#### 3.1. Microstructure analysis

The results of the XRD measurements are shown in Fig. 1. Samples after homogenization as well as after pre-annealing at several representative temperatures (mimicking the diffusion annealing treatments) were examined. The peaks observed in all XRD patterns correspond to a single-phase fcc structure with an average lattice parameter of about  $0.3555 \pm 0.0002$  nm. The result agrees well with literature data [45–47]. The absence of allowed peaks in the XRD pattern is due to the large grain size of the material, which allows the X-ray illumination of only a few grains ( $\sim 200$   $\mu\text{m}$ ). Note that different samples were examined, which explains the presence or absence of different XRD peaks, in addition to the main (111) peak, depending on the respective grain orientations. From these results it can be inferred that no additional phase originated during the annealing treatments, at least at the level of XRD sensitivity.

A representative EBSD map obtained on a sample annealed at 673 K for 168 h is shown in Fig. S1 (Supplementary Material). A coarse-grained microstructure is clearly visible and the average grain size is in excess of 200  $\mu\text{m}$ . This guarantees that the kinetic regimes of GB diffusion can correctly be identified (as discussed in the next section). It should be noted that the statistical reliability of the performed EBSD measurements for the grain size determination is not critical, as the actual value of the grain size does not affect the final results of the GB diffusion measurements. The corresponding strain maps in terms of the kernel average misorientation distribution, Fig. S2 in Supplementary material, substantiating the absence of significant accumulated stresses in the bulk of the sample.

The stability of the FCC phase at higher temperatures with respect to the elemental distribution has already been reported [48]. The FCC solid solution is thermodynamically unstable at lower temperatures, however it is kinetically stabilized at these temperatures [48]. Decomposition has been observed, e.g., at 773 K in CoCrFeMnNi only after prolonged annealing for 500 days [49]. Since the C-type kinetic measurements are intended at low temperatures, the stability of the FCC solid solution during diffusion annealing treatments has been investigated. Energy dispersive X-ray spectroscopy (EDS) analyses of the CoCrFeNi samples were conducted after annealing at 673 and 773 K, as shown in Fig. 2. As can be seen from the EDS elemental maps, no GB segregation can be observed after annealing at both temperatures at the resolution of the EDS measurements.

Since no precipitation or segregation could be discerned at the micrometre scale, even by a detailed SEM examination, nano-scale elemental investigation was carried out using APT measurements with a particular focus on potential phase transformations at grain boundaries. Fig. 3 presents the three-dimensional distribution of the constituent elements (Fe, Ni, Co and Cr) at the selected high-angle GB after annealing at 673 K for 168 h. All the elements are found to be homogeneously and randomly distributed within the analysed volume. A 1D concentration profile obtained along the 10 nm cylindrical region of interest further confirms a uniform distribution of the elements without any apparent compositional modulations. The SEM image (as inset) highlights the GB region from which the APT tips were prepared at specific locations on the boundary (highlighted by a rectangle) indicating that there is no preferential segregation at the grain boundary.

#### 3.2. Radiotracer measurements

The penetration profiles of GB diffusion are analysed according to the relevant kinetic regimes as classified by Harrison for polycrystalline materials [50], out of which the B- and C-type regimes are relevant for the present experimental conditions.

##### 3.2.1. B-type kinetic regime

The Le Claire parameter  $\alpha$ ,

$$\alpha = \frac{s\delta}{2\sqrt{D_v t}}, \quad (1)$$

is used to demarcate the B- and C-type kinetic regimes [51]. Here,  $t$  is the time of diffusion annealing,  $D_v$  is the volume diffusion coefficient,  $s$  is the segregation factor (generally unknown), and  $\delta$  is the GB width. The B-type regime is valid if  $\alpha < 0.1$  and a further parameter  $\Lambda$ ,

$$\Lambda = \frac{d}{\sqrt{D_v t}}, \quad (2)$$

is larger than about 3 [52] ( $d$  is the grain size). The two parameters confirm that the volume diffusion length is larger than the effective GB width,  $s \cdot \delta$ , but is smaller than the grain size,  $d$ . Hence, there is no overlap of fluxes in the crystalline bulk originating from different GBs. The solute segregation factor,  $s$ , is generally expressed as

$$s = \frac{c_{\text{gb}}}{c_v^0}, \quad (3)$$

where  $c_{\text{gb}}$  and  $c_v^0$  are the solute concentrations at a GB and in the bulk lattice, respectively. Since the tracer concentration is typically very small in a radiotracer experiment, it is reasonable to assume that the chemical element concentrations at a GB and in the bulk of the alloy determine the equilibrium segregation factor [12]. At elevated temperatures ( $> 1000$  K), the CoCrFeNi HEA exhibits a uniform composition without any solute enrichment [35]. Thus, for the initial estimates of the diffusion annealing times at the different temperatures, the value of  $s$  can safely be taken as unity. For many FCC metals and alloys, it was shown that the diffusional GB width  $\delta = 0.5$  nm is a reliable estimate [53] and this value holds true for the CoCrFeNi HEA as well, see below.

The B-type regime is typically characterized by two distinct branches in the penetration profiles, which allows the separation of bulk (near surface) and GB diffusion (tail) contributions [10]. In order to analyse the penetration profiles, numerical approximations of the exact solution of the Fisher model [54] provided by Le Claire [55] are typically used, as detailed by Kaur et al. [10].

Fig. 4 exemplifies the profiles measured at 1173 K and 1273 K in the B-type regime for Co, Cr, Fe and Mn tracers. It should be noted that Co, Cr and Fe represent self-diffusion cases (and correspondingly  $s \approx 1$ ), while Mn diffusion is considered as impurity diffusion and  $s_{\text{Mn}} \neq 1$ .

The near-surface branches of the profiles follow the Gaussian solution for the instantaneous source initial conditions [10] and the deeper branches of the diffusion profiles originate from grain boundary

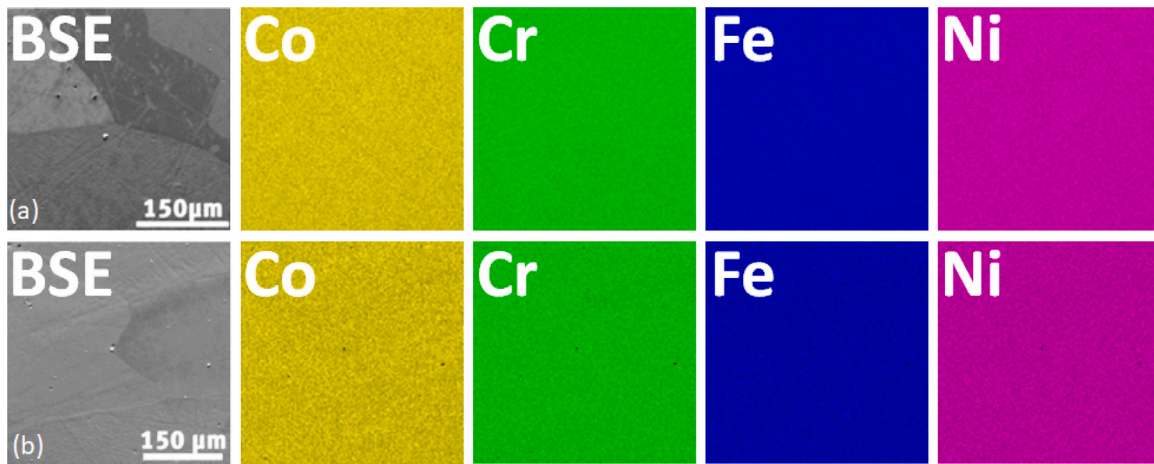


Fig. 2. The elemental EDS maps of the areas shown in back-scattered electron (BSE) images for samples of CoCrFeNi annealed for 5 days at (a) 673 K and (b) 773 K.

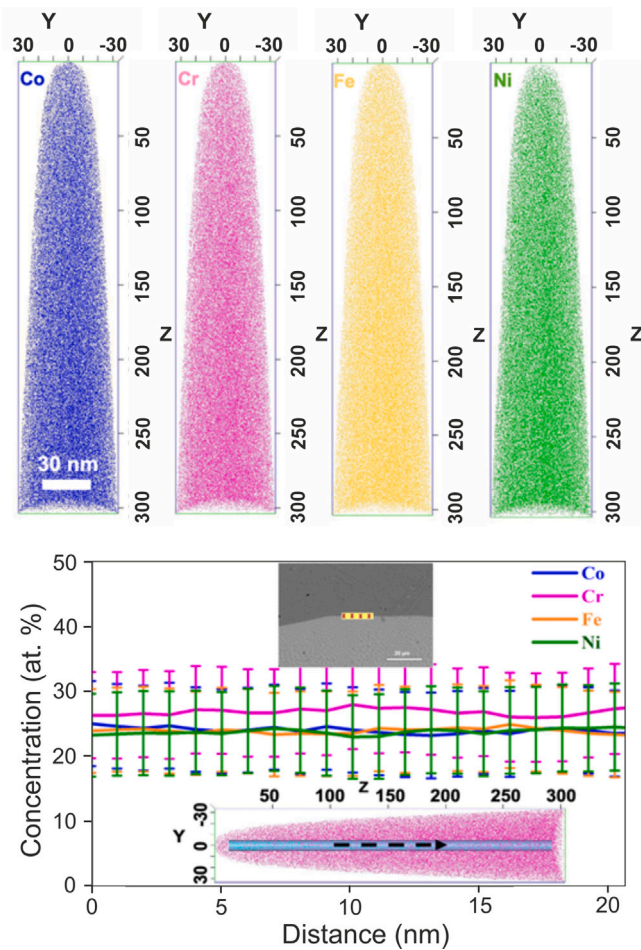


Fig. 3. 3D elemental distribution map of Co, Cr, Fe and Ni along with the 1D concentration profile obtained along a 10 nm diameter cylindrical region of interest with 0.5 nm bin width. The inset SEM image highlights the grain boundary location (rectangle) from which the site-specific APT tips were prepared for the analysis.

diffusion and follow approximately the  $\ln \bar{C} \sim x^{1.2}$  dependency [55]. Here  $\bar{C}$  is the tracer concentration averaged over a sectioned layer at the depth  $x$ . Thus, following expression is used to approximate the diffusion profiles,

$$\bar{C} = A_v \exp(-B_v x^2) + A_{gb} \exp(-B_{gb} x^{1.2}) \quad (4)$$

where  $A_v$ ,  $B_v$ ,  $A_{gb}$ , and  $B_{gb}$  are the corresponding fit parameters. According to Le Claire's analysis of Suzuoka's [56] exact solution of GB diffusion from an instantaneous source, it is the triple product  $P$ ,

$$P = s\delta D_{gb} = 1.322 \sqrt{\frac{D_v}{t}} \left( -\frac{\partial \ln \bar{C}}{\partial x^{6/5}} \right)^{-5/3} \quad (5)$$

which can be obtained from the corresponding slope of the GB diffusion-related branch of the penetration profile plotted in the coordinates of  $\ln \bar{C}$  vs.  $x^{1.2}$ . Equation Eq. (5) can be used if the second Le Claire parameter  $\beta$  [55],

$$\beta = \frac{P}{2D_v \sqrt{D_v t}} \quad (6)$$

is large enough, i.e.  $\beta > 10^4$  [10]. Somewhat modified expressions have to be used instead of Eq. (5) at smaller values of  $\beta$  [10]. Bulk diffusion coefficients,  $D_v$ , are required to determine the triple product  $P$  according to Eq. (5). In the present work, the bulk diffusion coefficients measured in dedicated experiments on CoCrFeNi single crystals [57] are used. The experimental parameters and the determined triple products are listed in Table 1. Since the present experiments were focused on GB diffusion measurements, the accuracy of the derived volume diffusion data is considered to be relatively low and they are not reported here. Still, these data agree generally well with the literature.

For the profiles with  $\beta < 10$ , the exact Suzuoka solution [56] was applied and the triple products were determined, with the corrections being less than 15% in the present case. If  $\beta > 10$ , the approximate Le Claire solutions provide sufficiently accurate results with respect to the experimental uncertainties. The latter do not exceed 10% in the present work.

### 3.2.2. C-type kinetic regime

The C-type kinetic regime holds when  $\alpha > 1$  [51], which corresponds typically to lower temperatures and/or shorter annealing times. The high value of  $\alpha$  suggests that the bulk diffusion depths are much smaller than the effective grain boundary width  $s \cdot \delta$  and bulk diffusion is effectively frozen in this regime. Thus, the GB diffusion coefficient,  $D_{gb}$ , can directly be determined using the Gaussian solution function for the instantaneous diffusion source problem [51],

$$D_{gb} = \frac{1}{4t} \left( -\frac{\partial \ln \bar{C}}{\partial x^2} \right)^{-1} \quad (7)$$

The penetration profiles for Co, Cr, Fe and Mn tracers measured at 643, 673 and 703 K are shown in Fig. 5a–d, respectively.

Similar to the previously observed trends for GB diffusion in the C-type kinetic regime for five-component CoCrFeMnNi HEA [35], all the profiles for CoCrFeNi reveal two distinct short-circuit contributions

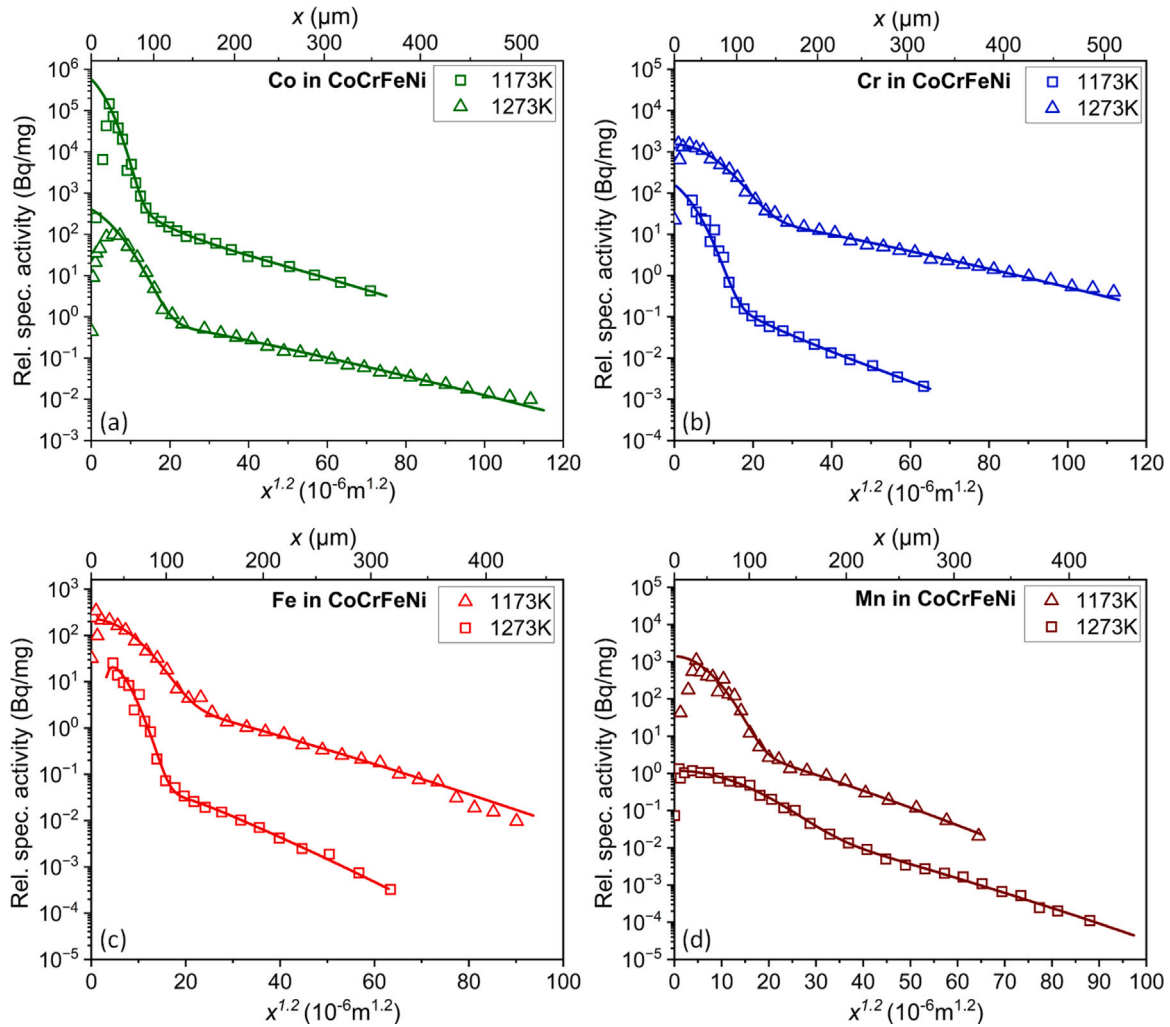


Fig. 4. Penetration profiles determined in the B-type kinetic regime at 1173 K and 1273 K for Co (a), Cr (b), Fe (c) and Mn (d). The profiles measured at 1173 K have been re-scaled for all tracers multiplying the depths to the 6/5th power by a factor of 4 and the relative specific activities by a factor of 0.001 for better visualization.

Table 1

Parameters of B-type kinetics measurements in CoCrFeNi for Co, Cr, Fe and Mn tracers. Note that the values of the parameter  $\alpha$  for all elements are calculated assuming the corresponding segregation factors as equal to unity,  $s = 1$ .

$T$ (K)	$t$ ( $10^4$ s)	Tracer	$\sqrt{D_v t}$ ( $\mu\text{m}$ )	$P$ ( $\text{m}^3/\text{s}$ )	$\alpha$	$\beta$	$A$
973	25.92	Co	0.08	$6.21^{+3.5}_{-2} \times 10^{-23}$	$3.17 \times 10^{-3}$	16364	2534
		Cr	0.12	$6.52^{+1}_{-0.6} \times 10^{-23}$	$2.14 \times 10^{-3}$	5280	1710
		Fe	0.11	$8.17^{+4.1}_{-2} \times 10^{-23}$	$2.20 \times 10^{-3}$	7190	1758
		Mn	0.11	$2.5^{+1.1}_{-1.3} \times 10^{-22}$	$2.21 \times 10^{-3}$	22331	1766
1073	25.92	Co	0.39	$6.36^{+2}_{-3.2} \times 10^{-22}$	$6.44 \times 10^{-4}$	1407	515
		Cr	0.66	$3.49^{+1.8}_{-1.4} \times 10^{-22}$	$3.81 \times 10^{-4}$	161	305
		Fe	0.60	$4.09^{+1.3}_{-1.3} \times 10^{-22}$	$4.18 \times 10^{-4}$	247	334
		Mn	0.65	$5.07^{+1.5}_{-2.3} \times 10^{-21}$	$3.86 \times 10^{-4}$	2426	309
1173	8.64	Co	0.84	$4.93^{+2}_{-1.5} \times 10^{-21}$	$2.97 \times 10^{-4}$	358	238
		Cr	1.58	$4.92^{+1}_{-0.9} \times 10^{-21}$	$1.58 \times 10^{-4}$	54	127
		Fe	1.37	$4.67^{+0.5}_{-1.5} \times 10^{-21}$	$1.82 \times 10^{-4}$	78	146
		Mn	1.59	$2.12^{+0.5}_{-1.5} \times 10^{-20}$	$1.58 \times 10^{-4}$	229	126
1273	25.92	Co	4.44	$1.69^{+0.3}_{-0.35} \times 10^{-20}$	$5.64 \times 10^{-5}$	25	45
		Cr	9.14	$3.42^{+0.37}_{-0.39} \times 10^{-20}$	$2.74 \times 10^{-5}$	6	22
		Fe	7.58	$2.48^{+0.3}_{-0.21} \times 10^{-20}$	$3.30 \times 10^{-5}$	1	26
		Mn	9.29	$1.02^{+0.1}_{-0.6} \times 10^{-19}$	$2.69 \times 10^{-5}$	16	22

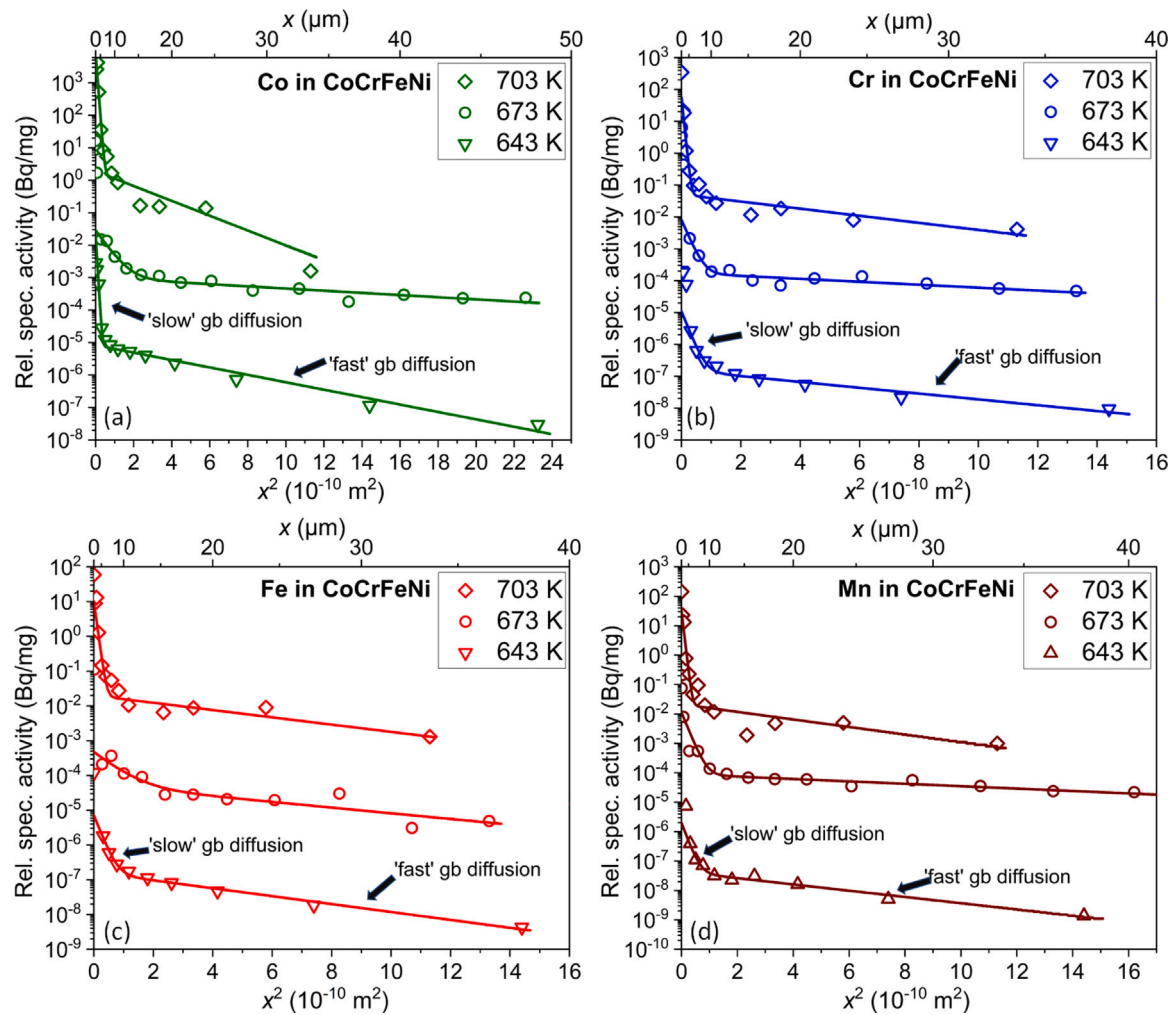


Fig. 5. Penetration profiles determined in the C-type kinetic regime at 643, 673 and 703 K for Co (a), Cr (b) and Fe (c). For better visibility, the profiles measured at 643 K have been re-scaled for all tracers by multiplying the  $x^2$  values by a factor of 4 and the relative specific activities by a factor of  $10^{-3}$  and for the profiles measured at 673 K only the relative specific activities were re-scaled by multiplying by a factor of  $10^{-6}$ . Consistently, two types of short-circuit contributions can be distinguished for the penetration profiles under C-type conditions, which are termed as 'slow' and 'fast' GB.

for depths larger than 5  $\mu\text{m}$ . The mechanical sectioning procedure used may induce some artefacts for very near-surface sections at depths below few micrometres and these points are not included in the analysis. The appearance of the two contributions hints towards the existence of two distinct types of high-angle GBs being present in the alloys and featuring different GB diffusion rates. Table 2 substantiates that the measurements were definitely carried out in the C-type kinetic regime,  $\alpha > 1$ , and therefore, a sum of two Gaussian-type solutions was used to fit the profiles,

$$\bar{C} = A_{gb1} \exp\left(-\frac{x^2}{4D_{gb1}t}\right) + A_{gb2} \exp\left(-\frac{x^2}{4D_{gb2}t}\right) \quad (8)$$

providing two diffusion coefficients for each profile and tracer,  $D_{gb1}$  and  $D_{gb2}$ .

#### 4. Discussion

The microstructure stability during diffusion annealing treatments has to be carefully evaluated in order to apply correct solutions of the diffusion equations and, hence, to deduce the reliable diffusivities.<sup>1</sup>

<sup>1</sup> GB motion, e.g., can modify the penetration profiles and its effect, if present, has to be carefully evaluated [51].

The XRD measurements and the EBSD analysis substantiated a single phase FCC structure which remains stable (at a micrometre scale) during the diffusion annealing treatments. The absence of bulk strain fields was also substantiated, see Fig. S2(b) in Supplementary Material. The temperature of 673 K was particularly considered for the phase stability, as the literature studies have often shown that the initially single-phase HEAs are susceptible to phase decomposition at low temperatures after prolonged annealing at moderate temperatures below 773 K [42,49,58]. The phase decomposition is significantly enhanced by a prior plastic deformation [59], which is thought not relevant for the present study since the samples were carefully annealed at elevated temperatures for stress relaxation.

The present GB diffusion measurements were performed on a polycrystalline material homogenized first at a relatively high temperature of 1373 K and annealed subsequently at the temperatures of the intended diffusion experiments. Even a well-equilibrated polycrystal is characterized by a broad spectrum of different GBs, ranging from low-angle to high-angle interfaces and a given fraction of special, low-sigma GBs. However, typical GB diffusion measurements indicate a major contribution of a single family of high-angle GBs featuring almost theoretically ideal shape of the penetration profiles [60,61], like the B-type profiles in the present study.

The reason is the way of the tracer diffusion measurements using precision parallel sectioning, in which we are averaging the tracer

**Table 2**

Parameters of C-type kinetic measurements in CoCrFeNi for Co, Cr, Fe and Mn tracers. Note that the values of the parameter  $\alpha$  for all elements are calculated assuming the corresponding segregation factors as equal to unity,  $s = 1$ .

$T$ (K)	$t$ ( $10^4$ s)	Tracer	$\sqrt{D_v t}$ (nm)	$D_{gb1}$ ("slow") ( $m^2/s$ )	$D_{gb2}$ ("fast") ( $m^2/s$ )	$\alpha$
643	86.40	Co	0.02	$1.78^{+1.1}_{-1.5} \times 10^{-18}$	$2.90^{+2.1}_{-2.3} \times 10^{-17}$	11.2
		Cr	0.02	$1.36^{+1.2}_{-1.3} \times 10^{-18}$	$3.44^{+2}_{-2.6} \times 10^{-17}$	15.5
		Fe	0.02	$1.46^{+1.3}_{-1.1} \times 10^{-18}$	$2.76^{+1.5}_{-2.2} \times 10^{-17}$	11.3
		Mn	0.01	$1.25^{+1.5}_{-1.4} \times 10^{-18}$	$2.95^{+1.9}_{-2.1} \times 10^{-17}$	17.8
673	60.48	Co	0.06	$1.97^{+1.6}_{-1.3} \times 10^{-17}$	$3.66^{+2}_{-3} \times 10^{-16}$	4.2
		Cr	0.05	$8.37^{+1.2}_{-1.1} \times 10^{-17}$	$3.92^{+2.1}_{-3.2} \times 10^{-16}$	5.3
		Fe	0.06	$3.18^{+1.9}_{-2.1} \times 10^{-17}$	$4.93^{+3.1}_{-3.3} \times 10^{-16}$	4.1
		Mn	0.04	$1.71^{+1.5}_{-1.4} \times 10^{-17}$	$5.26^{+1.9}_{-2.5} \times 10^{-16}$	6.1
703	8.64	Co	0.06	$5.03^{+1.1}_{-2.2} \times 10^{-17}$	$4.61^{+0.8}_{-0.6} \times 10^{-16}$	3.9
		Cr	0.06	$4.90^{+1.3}_{-1.9} \times 10^{-17}$	$1.67^{+0.9}_{-0.1} \times 10^{-15}$	4.5
		Fe	0.07	$6.10^{+1.3}_{-1.1} \times 10^{-17}$	$1.10^{+0.6}_{-0.6} \times 10^{-15}$	3.6
		Mn	0.05	$6.19^{+1}_{-1.2} \times 10^{-17}$	$2.17^{+0.7}_{-0.9} \times 10^{-15}$	5.1

concentrations created by diffusion along the available GBs. The low-angle or low-sigma (aka twin) GBs feature typically relatively low diffusion rates [61] resulting in some tracer accumulation in the near-surface sections which could hardly be resolved from direct diffusion along the crystalline bulk. The deepest sections provide clearly resolved GB diffusion contributions and the corresponding diffusion rates are reported as GB diffusivities for the polycrystalline material, see Fig. 4. However, the concentration profiles measured under the C-type kinetics reveal an "anomalous" shape, Fig. 5, which has to be discussed in detail.

#### 4.1. Two diffusion contributions in the C-type kinetics: Hints towards phase transformations at grain boundaries

The penetration profiles measured under the C-type kinetic conditions show two distinct contributions and the origin of these two contributions has to be understood.

In order to reflect the general complexity of the problem, potential scenarios are listed below. It must be noted that we limit the discussion to the C-type kinetics of tracer GB diffusion after Harrison's classification for completely relaxed and recrystallized polycrystal, otherwise the list would be longer.

1. Parallel and independent contributions of several (in the particular case, two of them) short-circuit paths as discovered and analysed, e.g., by Beke et al. [62];
2. A hierarchy of interfaces with a complex geometrical arrangement and strongly different diffusivities as analysed by Divinski et al. [52,63,64];
3. simultaneous contributions of dislocation and GB diffusion transport as analysed by Klinger and Rabkin [65] or Divinski et al. [66].

As it was mentioned, although the samples contain a spectrum of high-angle/low-angle/ low-sigma grain boundaries, the contributions of the low-angle and low-sigma GBs are probably not resolved in the present experimental conditions, since the diffusion rates along these interfaces are significantly lower than those along the random high-angle grain boundaries in typical conditions [51,61]. We also rule out dynamic recrystallization during the diffusion annealing at low temperatures since the samples used for these measurements were already sufficiently heat-treated at higher temperatures.

Scenarios 2 and 3 imply a high density of slow-diffusion short-circuit paths which would require a specific analysis of the diffusion rates along the fast-diffusion short circuits [52,64,65]. Such hypothetical arrangements can safely be ruled out in the present case in view of a coarse microstructure with a relatively low density of the potential short circuits.

Thus, we are inclined to conclude that two families of GBs with different kinetic properties appear in the alloy under the conditions of the C-type kinetics (note that at least one of those families is absent at higher temperatures under the B-type conditions) and they provide parallel and independent contributions according to Scenario 1.

The two contributions to the penetration profiles are attributed to diffusion along these two distinct families of grain boundaries revealing the  $D_{gb1}$  and  $D_{gb2}$  diffusivities (determined according to Eq. (8)). In Fig. 6, the triple products  $P$  and the GB diffusion coefficients  $D_{gb1}$  and  $D_{gb2}$  measured under the B- and C-type kinetic conditions, respectively, are compared. For an appropriate comparison, the measured diffusion coefficients are multiplied by the GB diffusion width  $\delta$  taken as 0.5 nm.

One immediately observes that the triple products  $P$  measured at high temperatures and the product  $s \cdot \delta \cdot D_{gb1}$  reasonably follow the same Arrhenius-type temperature dependence over many orders of magnitude. This behaviour holds systematically for all isotopes, Fig. 6. Thus one may safely conclude that  $s \cdot \delta \approx 0.5$  nm for all isotopes for the interfaces which are characterized by the  $D_{gb1}$  values. This conclusion is fully supported by the absence of GB segregation/depletion as revealed by APT examination, Fig. 3. Therefore, the  $P$  and  $D_{gb1}$  values can safely be interpreted as the characteristic diffusion parameters for general (random) high-angle GBs.

The family of grain boundaries which are responsible for the  $D_{gb2}$  contribution provides a room for interpretation. Firstly, Fig. 6 suggests that hypothetical diffusivities of the " $D_{gb2}$ -interfaces" at high temperatures have to be faster than those of the " $D_{gb1}$ -interfaces", as a simple extrapolation to the high temperatures would predict. However, any "faster" contribution to the B-type penetration profiles can safely be excluded, since all profiles were processed till the background was approached and only a single contribution was measured (the corresponding  $P$  values are shown as open circles Fig. 6). Thus, we can conclude that the interfaces, which are characterized by the diffusion coefficients  $D_{gb2}$ , are not present at the high temperatures under the B-type kinetic conditions.

Since the radiotracer technique is an integral one, we cannot tag a specific GB (or a GB family) being responsible for the accelerated mass transport which is characterized by the  $D_{gb2}$  value. A combination of a quantitative sectioning analysis and an autoradiography would be a possible method to localize the planar defects being responsible for the deep tracer penetration, see e.g. the analysis of the interconnected porosity in a Cu-Pb alloy [67]. However, the radioactive samples cannot subsequently be used for a local microstructure examination. On the other hand, any atomic-scale investigation e.g. with atom probe tomography or high-resolution transmission electron microscopy remains highly local and the success of locating a grain boundary of the second family corresponding to the  $D_{gb2}$  values is unpredictable. A most straightforward explanation for  $D_{gb2}$  is to rely on the same phenomenon which was discovered, both via diffusion analysis like in the present

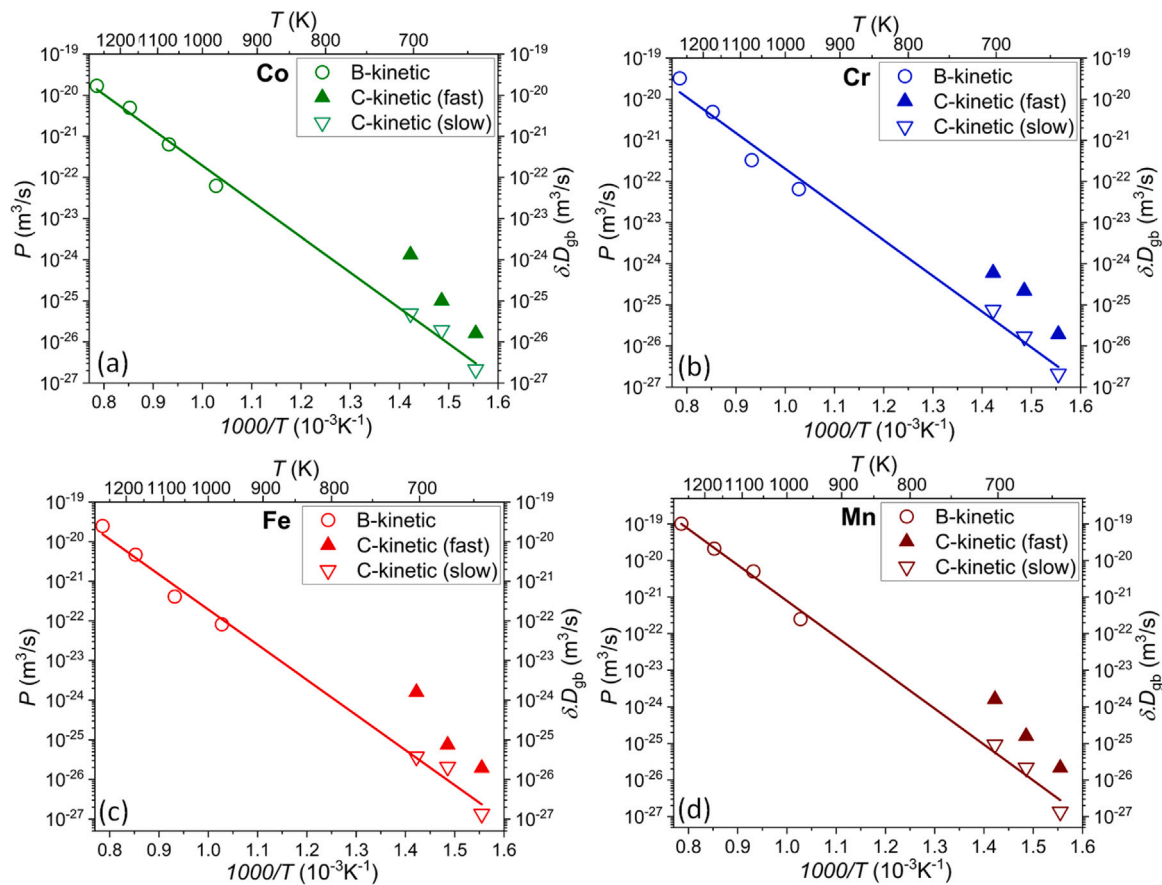


Fig. 6. Arrhenius plots for the diffusion of Co (a), Cr (b), Fe (c) and Mn (d) determined in the B-type (the triple products  $P$ , open circles, left ordinate) and C-type (the products of the measured diffusion coefficients  $D_{gb_1}$ ,  $D_{gb_2}$  and of the GB width  $\delta = 0.5$  nm, triangles, right ordinate) kinetics regimes.

case and via direct microstructure observations, in the five-component Cantor alloy [35]. In particular, the  $D_{gb_2}$  contribution was related to the nucleation of nano-sized precipitates at a fraction of high-angle GBs already after 14 d annealing at 700 K [35]. Although, the present study using the atom probe tomography did not localized GB precipitates in the CoCrFeNi system, there exist numerous indications in favour of such explanation.

For the four-component CoCrFeNi system, Bracq et al. [48] predicted the appearance of a BCC (Cr-rich) phase below 900 K, a second FCC phase (Ni-rich) below 830 K and a second BCC phase (CoFe-rich) below 700 K (as bulk equilibrium phases) while for the five-component CoCrFeMnNi, the appearance of a Cr-rich sigma phase (below 900 K), a NiMn-rich  $L1_2$  and a CoFe-rich BCC (B2) phase was predicted. Experimentally, the predicted phase decomposition was indeed observed for the CoCrFeMnNi alloy after very prolonged annealing by Otto et al. [49], with second-phase particles grown to the micrometre scale. The kinetics of decomposition was found to be slow, but at GBs it is enhanced due to enhanced GB diffusion rates and the occurrence of heterogeneous nucleation. Similar to the previous findings for the quinary CoCrFeMnNi system [35], we attribute the second “fast” contribution in the C-type kinetics regime in the CoCrFeNi system as corresponding to the high-angle GBs where the onset of phase decomposition leads to an increased level of strains/stresses which partially relaxes due to the formation of networks of secondary dislocations.

Bulk diffusion in the CoCrFeMnNi alloy was found to reveal a non-Arrhenius character, especially for slow diffusing elements (Co, Ni) [57], which was discussed in terms of potential short-range ordering. Since the existence of a phase decomposition in the CoCrFeMnNi alloy was directly shown previously [35], it is highly probably that these two phenomena are related. In the four-component CoCrFeNi, the

Arrhenius dependence of bulk diffusion remains linear and continuous down to 900–1000 K [57]. Still, the present measurements support a view of GB-related structure transformations below 700 K which may probably induce composition changes. A strong support for the occurrence of GB phase transformations is provided by simulations by Cao et al. for CoCrNi [68] or by Li et al. [69] for BCC HfTiZrTa (see also the recent paper by Luo and Zhou [39]). We are expecting that features similar to those observed by Glienke et al. [35] are applicable to the present CoCrFeNi system, too. Very recently, further hints towards element segregation/depletion at GBs in the CoCrFeNi were elaborated by Ma et al. [70].

To corroborate the data in the literature, we performed thermodynamic calculations for the CoCrFeNi–Mn pseudo-binary section of the CoCrFeMnNi system using the TCHEA6 database and applying the Thermo-Calc software [71,72] in order to compare the phase decomposition behaviour of CoCrFeNi and CoCrFeMnNi alloys and assess the potential phases which are suggested to appear at GBs, Fig. 7. A vertical dashed line in Fig. 7 indicates the 20% Mn composition, which corresponds to the equiatomic CoCrFeMnNi HEA. The temperature ranges of the B-type (973 K – 1273 K) and C-type (643–703K) GB diffusion measurements are also indicated in Fig. 7. While the FCC solid solution is stable within the temperature interval of the B-type kinetics diffusion measurements in CoCrFeNi, the calculations predict the formation of a Cr-rich  $\sigma$  phase below 1200 K in CoCrFeMnNi, Fig. 7. Yet, the GB diffusion measurements provided no indications for a phase decomposition on the time scale of days under these conditions according to Glienke et al. [35]. At the lower temperatures of the C-type kinetics measurements, the thermodynamic calculations do predict a decomposition. However, a phase separation in the crystalline bulk was not observed at the micrometre-scale after annealing for 14 days

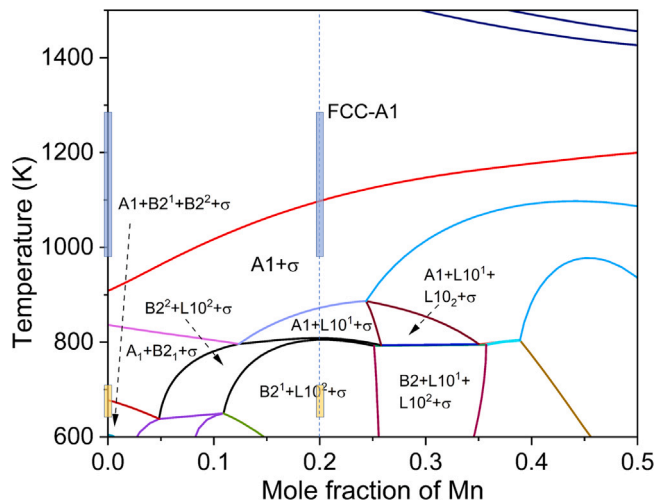


Fig. 7. Isoleth section calculated for the CoCrFeNi–Mn system using the TCHEA6 database and applying the ThermoCalc [72] software. The yellow and blue shaded regions represent the temperature intervals corresponding to the C-type and B-type kinetic diffusion regimes, respectively. (For interpretation of the references to colour in this figure legend, the reader is referred to the web version of this article.)

due to kinetic limitations, in full accordance with observations of Otto et al. [73].

In CoCrFeMnNi, nano-scale precipitates have been shown to form after prolonged annealing for 500 days [35,49], while GP zone-like clusters have been observed only during solid solution phase decomposition of CoCrFeNi [74]. A careful look at the phase diagram in Fig. 7 suggests that the FCC phase in CoCrFeNi is predicted to be stable down to much lower temperatures (900 K) as compared to CoCrFeMnNi. Further, it has also been shown that at the same absolute temperatures the diffusion rates in CoCrFeNi are lower than for CoCrFeMnNi [17,18]. Therefore, both the driving force for phase decomposition as well as the diffusion rates are lower in CoCrFeNi. These facts correlate with the observation that the second phase precipitates are not captured by the present APT analysis at all inspected GBs.

While nano-scale precipitates of Cr-rich  $\sigma$ , NiMn-rich  $L1_2$  and CoFe-rich B2 phases were observed in CoCrFeMnNi at some high-angle GBs after annealing for 14 days at 673 K [35], a smaller fraction of the Cr-rich  $\sigma$  phase and a dominating FeCo-rich BCC phase are predicted for CoCrFeNi at 673 K, Fig. 7.

We conclude that these GBs represented short-circuit paths featuring “slow” diffusion rates in the C-type kinetics regime. One may speculate about a low density of such GBs where a phase transformation occurred, that hinders a direct observation of a GB phase transformation by a local analysis. This assumption is corroborated by a careful examination of the tracer penetration profiles where we propose a new method to locate hints of grain boundary precipitation using diffusion penetration profiles.

In Fig. 8, the penetration profiles presently measured in CoCrFeNi are compared to those measured previously under *identical* conditions as for the CoCrFeMnNi alloys [35]. In all our experiments, a special care was taken to apply similar amounts of the tracer solution to the diffusion samples. Since the diffusion conditions corresponded to the C-type kinetics regime of GB diffusion with frozen bulk diffusion, the factors  $A_{gb_i}$  in Eq. (8) are proportional to the area fractions,  $f_i$ , of the pertinent short-circuit paths and under an approximation of cubic grains,

$$A_{gb_i} = \frac{M f_i}{\sqrt{\pi} D_{gb_i} t} \approx \frac{2M\delta}{d_i \sqrt{\pi} D_{gb_i} t}. \quad (9)$$

Here  $M$  is the amount of the tracer material deposited per unit area of the sample surface,  $\delta$  is the GB width (in a first approximation we are

Table 3

Arrhenius parameters for the B-type kinetics measurements fitted together with the “slow” C-type kinetics contribution for CoCrFeNi. The melting temperature ( $T_m$ ) of CoCrFeNi as 1717 K was used as reference temperature.

Tracer	$P_0$ $10^{-13} \text{ m}^3/\text{s}$	$Q_{gb}$ kJ/mol	$Q_{gb}^* = Q_{gb}/RT_m$	Ref.
Co	$0.87^{+0.75}_{-0.40}$	$165 \pm 4$	$11.6 \pm 0.3$	present work
Cr	$0.97^{+1.69}_{-0.62}$	$166 \pm 7$	$11.6 \pm 0.5$	present work
Fe	$1.39^{+1.89}_{-0.81}$	$169 \pm 6$	$11.9 \pm 0.4$	present work
Mn	$52.1^{+62}_{-28}$	$188 \pm 5$	$13.2 \pm 0.4$	present work
Ni	$0.11^{+0.07}_{-0.19}$	$158 \pm 7$	11.3	[17]

not distinguishing the widths of GBs representing the “slow” ( $i = 1$ ) or “fast” paths ( $i = 2$ )) and  $d_i$  is the average distance between the GBs within each family,  $i = 1, 2$ .

Graphically, the pre-factors  $A_{gb_i}$  in Eq. (8) correspond to the Y-axis intercepts of the corresponding branches, which are linear in the coordinates used in Figs. 8(a)–(d). Whereas  $A_{gb1}^{5C}/A_{gb1}^{4C} \approx 1$  for all tracers, the ratios  $A_{gb2}^{5C}/A_{gb2}^{4C}$  amount to about 100 (in fact, varying between 50 and 200 for different tracers), Figs. 8(a)–(d). Note that the different isotopes emit the  $\gamma$ -quanta with different energies; thus the corresponding decays are counted with different efficiencies and are affected by different background intensities. This explains the minor deviations of the  $A_{gb2}^{5C}/A_{gb2}^{4C}$  ratios for different isotopes.

A direct comparison of the present and previous [35] data corroborates that the ratios of the determined GB diffusion rates for the “slow” and “fast” branches in 4C and 5C alloys deviate from unity by a factor of two to three. Therefore, the findings  $A_{gb2}^{5C}/A_{gb2}^{4C} \sim 100$  and  $A_{gb1}^{5C}/A_{gb1}^{4C} \approx 1$  together suggest that the fraction of “fast” GBs in the 5C (CoCrFeMnNi) alloy exceeds that in the 4C (CoCrFeNi) alloy by about two orders of magnitude and explains an almost negligible chance for detecting the “fast” GBs in CoCrFeNi with such a highly local technique as APT.

#### 4.2. Temperature dependence of GB diffusion

The value of the GB width  $\delta = 0.5 \text{ nm}$  [53] was used in the present analysis. In Fig. 6, the temperature dependencies of the triple products,  $P$ , (measured in the B-type kinetic regime) and of the products of the GB diffusion coefficients (measured in the C-type kinetics regime) and the GB width  $\delta$ , i.e.  $\delta \cdot D_{gb_1}$  and  $\delta \cdot D_{gb_2}$  are plotted together. Typically, common Arrhenius-type temperature dependencies, solid lines, are found for the  $P$ -values and the products  $\delta \cdot D_{gb_1}$ , while the values of  $\delta \cdot D_{gb_2}$  lie consistently higher for all the four isotopes.

We interpret the contribution that lies on the Arrhenius line as having originated from diffusion along random high-angle GBs with equiatomic composition, as they exist at elevated temperatures. These results also validate the use of  $s \cdot \delta = 0.5 \text{ nm}$ , at least for Co, Cr and Fe representing self-diffusion, and allows us to extract the corresponding Arrhenius parameters, namely the pre-exponential factor,  $P_0$ , and the activation enthalpy,  $Q_{gb}$ , related by  $P = P_0 \exp(-Q_{gb}/RT)$ , and the results are given in Table 3. Thus, Co, Cr, and Fe, at least, do not strongly segregate at general high-angle GBs (“slow” branch) in CoCrFeNi. A certain enrichment/depletion of these elements may be expected at the high-angle GBs composing the “fast” diffusion branch and such evolution of the GB composition might induce phase decomposition at the interfaces [75].

The GB self-diffusivities (“slow”) of the individual tracers Co, Cr, and Fe studied in the present work and Ni GB diffusivities investigated previously in Ref. [34] are compared on the inverse absolute temperature scale in Fig. 9. Very similar diffusion coefficients are obtained for Co, Cr, and Fe, which are higher than the diffusivities of Ni in the same temperature range as shown in (Fig. 9).

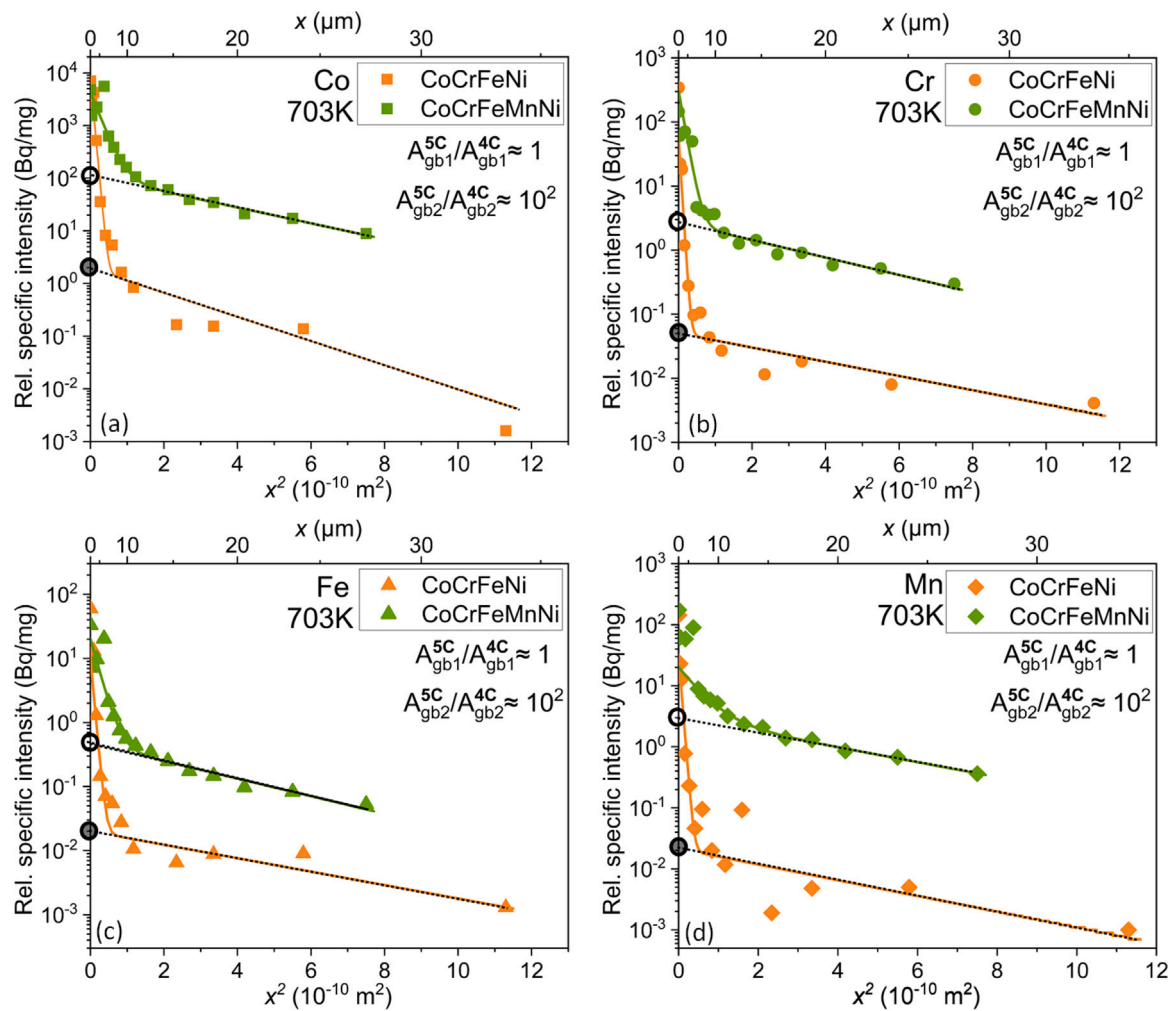


**Fig. 8.** Comparison of the C-type kinetics penetration profiles for CoCrFeNi (orange symbols) and CoCrFeMnNi [35] (green symbols) for Co (a), Cr (b), Fe (c), and Mn (d). The solid lines correspond to the approximations according to Eq. (8). The pre-exponential factors in Eq. (8),  $A_1$  and  $A_2$ , correspond to the Y-axis intercepts for the “slow” and “fast” contributions. The values of  $A_2^{5C}$  and  $A_2^{4C}$  are indicated as filled and open black circles, respectively. (For interpretation of the references to colour in this figure legend, the reader is referred to the web version of this article.)

Mn, which is an impurity element in CoCrFeNi, represents a special case. Generally, one may expect that the corresponding segregation factor is not unity as it was found for the constituent elements. However, a detailed APT inspection of general high-angle GBs annealed under conditions which mimic the C-type kinetics diffusion annealing treatments does not reveal any Mn segregation. This finding agrees with the result shown in Fig. 6(d) that the values of the triple products,  $P_{Mn}$ , lie on the same Arrhenius line as the values of the double products  $\delta \cdot D_{gb1}^{Mn}$ . We conclude that the Mn segregation factor for the general high-angle GBs representing the “slow” paths is about unity in CoCrFeNi.

In Fig. 9, the data for Mn are compared with the diffusivities measured for other elements and Mn is seen to exhibit higher diffusion rates as compared to the self-diffusion rates of the constituent elements.

#### 4.3. Impact of chemical complexity on GB diffusion in FCC alloys

In this section, the grain boundary diffusivities of Co, Cr and Fe measured in the CoCrFeNi system are compared with the diffusivities in other FCC systems, namely the relevant unary, binary, and ternary alloys and the quinary CoCrFeMnNi HEA in order to elaborate the impact of chemical complexity on the rates of GB diffusion.

The Arrhenius parameters of diffusion in these FCC systems are listed in Table 4 along with the temperature ranges in the original experiments and the bulk diffusivity parameters. The melting temperatures ( $T_m$ ) have been calculated using the TCHEA6 database with the

Thermocalc software Ref. [72]. It may be noted that we have used the liquidus temperatures  $T_m$  for all alloys, hence the choice does not influence the relative trends. All numbers denoted in the nomenclature of the alloys express the fractions of the elements (in wt.%) in that particular alloy. It is important to note that in systems that undergo allotropic transformations, e.g. Co, Fe, Fe-2.9Cr, only the FCC phase has been considered for the present comparison of the GB diffusion properties.

Using the parameters for the systems listed in Table 4, the grain boundary diffusivities are plotted as a function of the inverse absolute ( $1/T$ ) and inverse homologous ( $T_m/T$ ) temperatures in Fig. 10 individually for the Co, Cr and Fe.

Although we systematically compare the systems with an increasing chemical complexity from unary to quinary alloys, the discussion on “sluggish GB diffusion”, especially for the polycrystalline materials, is a very complex problem indeed, since GB diffusion is influenced by many different factors like particular misorientation [88] or inclination [89], elemental segregation [60], the presence of precipitates [90], GB defects (disconnections, steps and facets) and so on. However, there are some interesting trends that can be discerned from Fig. 10.

The diffusion “sluggishness” [16] is a loosely defined quantity which needs to be quantified. A rigorous definition has been proposed by Daw and Chandross [91] with a comparison of the vacancy diffusion rates in pure elements and in a given multi-component alloy. This

**Table 4**

List of grain boundary diffusivity parameters-  $P_0$ ,  $Q_{gb}$ , bulk diffusivity parameters  $D_0$  and  $Q_v$  (used for the evaluation of  $P_0$ ,  $Q_{gb}$ ), their respective temperature ranges, melting points and references. All compositions (excluding the equiatomic ones) are in wt.%. The numbers in brackets indicate material's purity.

Tracer	Alloy	Temp. range (K)	$T_m$ (K)	$P_0$ ( $m^3/s$ )	$Q_{gb}$ (kJ/mol)	$D_{v_0}$ ( $m^2/s$ )	$Q_v$ (kJ/mol)	Ref.
Co	$\gamma$ -Co	973–1273	1786	$2 \times 10^{-14}$	117	–	–	[76,77]
	CoCrFeNi	973–1273	1716	$8.70 \times 10^{-14}$	165	$1.7 \times 10^{-5}$	277	This work
	CoCrFeMnNi	973–1273	1591	$1.66 \times 10^{-12}$	181	$6 \times 10^{-4}$	303	[35]
Cr	Ni	1125–1352	1726	$1.0 \times 10^{-12}$	190	$8.6 \times 10^{-4}$	288.6	[78,79]
	Fe-2.9Cr	1100–1360	1806	$4.51 \times 10^{-14}$	147	$1.9 \times 10^{-5}$	262	[77,80]
	Ni-20Cr	1075–1515	1673	$7.60 \times 10^{-14}$	155	$6.0 \times 10^{-5}$	263	[77,81]
	Fe-17Cr-12Ni	849–1323	1731	$3.50 \times 10^{-14}$	152	$1.30 \times 10^{-5}$	264	[77,82]
	Fe-18Cr-10Ni	973–1323	1739	$4.4 \times 10^{-12}$	189	$1.44 \times 10^{-9}$	153	[77,83]
	CoCrFeNi	973–1273	1716	$9.70 \times 10^{-14}$	166	$6.1 \times 10^{-4}$	299	This work
	CoCrFeMnNi	973–1273	1591	$1.43 \times 10^{-12}$	181	$7.2 \times 10^{-4}$	295	[35]
Fe	$\gamma$ -Fe (2N7)	1196–1289	1811	$6.79 \times 10^{-13}$	174	$1.85 \times 10^{-6}$	251	[77,84]
	$\gamma$ -Fe (4N)	1191–1287	1811	$9.03 \times 10^{-13}$	180	$1.85 \times 10^{-6}$	251	[77,84]
	$\gamma$ -Co	1125–1352	1786	$5.6 \times 10^{-15}$	131	$2.8 \times 10^{-8}$	174.5	[85]
	Ni	850–1208	1726	$1.3 \times 10^{-12}$	174	$9.5 \times 10^{-4}$	296.5	[78]
	Fe-2.9Cr	1100–1346	1806	$9.0 \times 10^{-16}$	109	$5.15 \times 10^{-7}$	218	[77,80]
	Ni-Co <sup>a</sup>	1196–1255		$2.76 \times 10^{-11}$	221	$1.6 \times 10^{-5}$	247	[86]
	Fe-17Cr-12Ni	870–1306	1731	$5.30 \times 10^{-13}$	177	$3.70 \times 10^{-5}$	279	[77,82]
	Fe-18Cr-10Ni	1123–1323	1739	$2.96 \times 10^{-13}$	204	$4.40 \times 10^{-5}$	280	[77,83]
	Ni-20Cr-15Fe	1018–1073	1682	$3.20 \times 10^{-11}$	234	$1.0 \times 10^{-4}$	272	[77,87]
	CoCrFeNi	973–1273	1716	$1.39 \times 10^{-13}$	169	$1.5 \times 10^{-4}$	288	This work
CoCrFeMnNi	973–1273	1591	$1.40 \times 10^{-12}$	182	$3.2 \times 10^{-5}$	264	[35]	

<sup>a</sup> The exact composition of the Ni-Co alloy was not specified in that study.

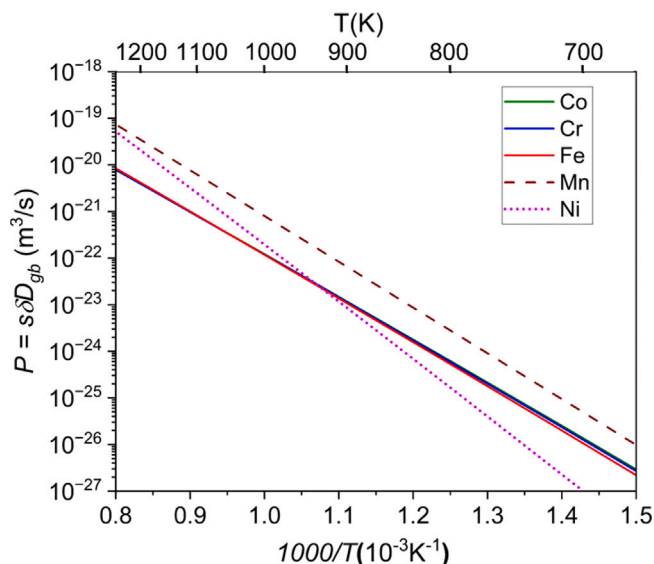


**Fig. 9.** Comparison of diffusivities of the individual tracers Co, Cr, Fe and Mn (this work) and Ni [34] in polycrystalline CoCrFeNi HEA.

definition can be used in atomistic simulation, but it is at least quite involved to measure the vacancy diffusion coefficients, especially in pure elements with a metastable crystallographic lattice dictated by the given alloy. Zhang et al. [28] and Sen et al. [22] have suggested to compare the geometric mean of the tracer diffusion coefficients of the given element in all unaries with the corresponding diffusion rate in the multi-component alloy.

Following the same, experimentally-driven approach, we may compare the accessible triple product values  $P$  for selected elements in available unaries with the GB diffusivities in multi-component alloys. A most valuable comparison can be done for Fe diffusion in FCC metals and alloys, Fig. 10(c). An increased chemical complexity does not influence monotonically the GB diffusivities. Whereas a strong retardation of the Fe GB diffusion rate in the Fe-based ternary alloys is pronounced,  $P_{Fe}$  is higher in CoCrFeNi at the same absolute temperature and in CoCrFeMnNi it corresponds to the geometric mean of the  $P$  values

measured for available pure elements. On the other hand, the Cr GB diffusion rates are very similar for all FCC matrices, Fig. 10(b), and a strong retardation of the Co GB diffusion rate is seen, Fig. 10(a).

Therefore, the experimentally available information does not provide an unambiguous support towards inevitable “sluggishness” of GB diffusion in the polycrystalline FCC alloys. This comparison has to be used with caution since the  $P = s \cdot \delta \cdot D_{gb}$  values are compared and hypothetically a decrease of the GB diffusion coefficient  $D_{gb}$  can be “masked” by an increase of the corresponding segregation factor  $s$ . The C-type GB diffusion measurements, which would provide the  $D_{gb}$  values, are extremely rare and presently the results are available for few systems only.

On the homologous temperature scale, Figs. 10(d)–(f), the results are more systematic. Co diffusivities in the unary  $\gamma$ -Co are higher than in the quinary CoCrFeMnNi and quaternary CoCrFeNi HEAs, the latter exhibiting similar GB diffusion rates, with Co diffusing slightly faster in the CoCrFeNi system, Fig. 10(d). With respect to the Cr tracer, Fig. 10(e), both HEAs (CoCrFeNi and CoCrFeMnNi) have the lowest diffusivities among all systems with the highest diffusivity being exhibited by the binary Fe-2.9Cr system. Fe diffuses fastest in the unary  $\gamma$ -Fe, but no straightforward trend in the GB diffusivity can be detected for the higher order alloys, Fig. 10(e).

The comparative analysis presented here is a qualitative one, since an accurate quantitative comparison of the GB diffusivities is not straightforward. To highlight the complexity of a direct comparison for discussing GB diffusivity, we consider two systems, namely  $\gamma$ -Fe (7N2 and 4N purity) and the Fe-rich ternary systems (Fe-17Cr-12Ni and Fe-18Cr-10Ni). In the unary  $\gamma$ -Fe, keeping all parameters equal, the GB diffusivity seems to be slower for the sample with a higher purity. This is in a clear contradiction to the generally observed phenomenon that GB diffusivity increases with increasing purity in the unary systems, as observed for Ni [53,92],  $\alpha$ -Fe [66] and Cu [93,94]. It is not just the amount of impurity, but also the type of impurity present that can influence GB diffusion. In the ternary Fe-17Cr-12Ni and Fe-18Cr-10Ni systems, although the chemical composition of both the alloys is rather similar, the trends in the GB diffusivities are widely different for Cr and Fe. Cr diffuses faster in the Fe-18Cr-10Ni alloy as compared to the Fe-17Cr-12Ni alloy. This trend is however reversed for Fe diffusion. While an impurity level of less than 50 ppm was reported for the Fe-18Cr-10Ni [83], the impurity levels in the Fe-17Cr-12Ni system were not specified but it was mentioned that a presence of impurities could have

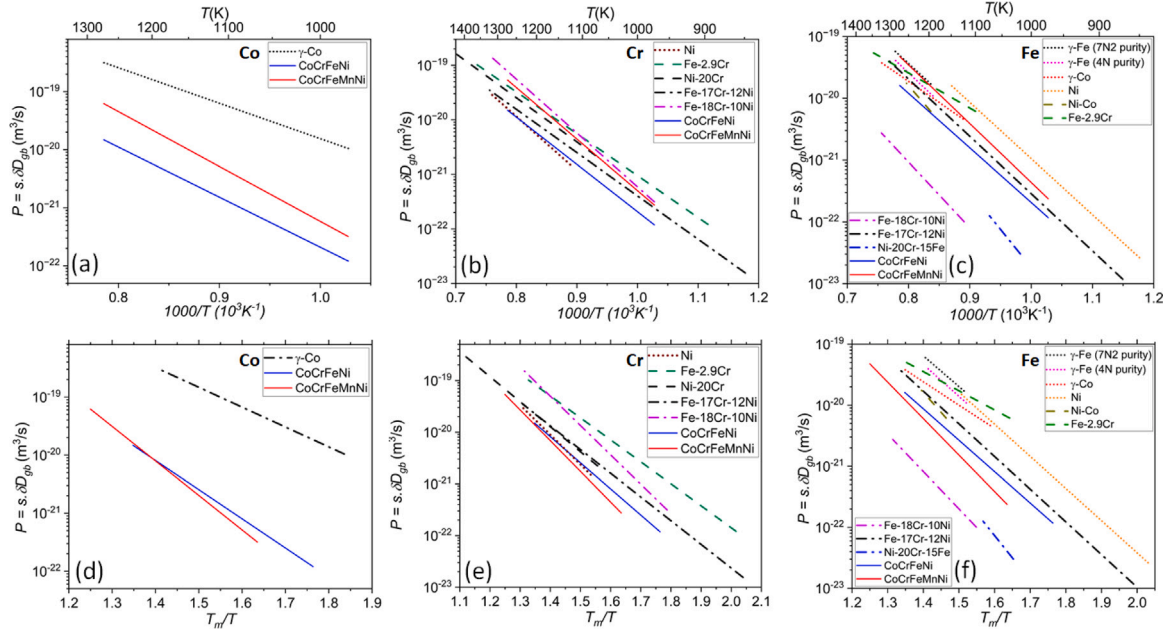


**Fig. 10.** Comparison of the triple products,  $P$ , for Co (a, d), Cr (b, e), and Fe (c, f) measured in CoCrFeNi (blue solid line, the present work) with the diffusion data for other FCC systems. The diffusion rates are compared using the inverse homologous temperature (a–c) or inverse absolute temperature (d–f) scales. The available literature data on GB diffusion in unary, binary and ternary alloys are shown using dotted, dashed, and dotted-dashed lines, respectively; and the GB diffusivities in CoCrFeMnNi are plotted using red solid lines. The Arrhenius parameters and references are listed in Table 4. (For interpretation of the references to colour in this figure legend, the reader is referred to the web version of this article.)

lead to such a large difference in the GB diffusivities as observed for Cr and Ni in this alloy [82]. Even for the two HEA systems, two distinct contributions were observed at lower temperatures, owing to phase decomposition at grain boundaries, which influences GB diffusion in addition to the impurities like C and S.

#### 4.4. Grain boundary energy

Grain boundary energy is an important parameter for many properties associated with pure metals as well as alloys. Borisov et al. [95] proposed a semi-empirical correlation between the grain boundary energy,  $\gamma_{gb}$ , and the relative enhancement of the GB self-diffusion coefficient,  $D_{gb}$ , with respect to the volume self-diffusion coefficient,  $D_v$ ,

$$\gamma_{gb} = \frac{RT}{2a^2 N_a} \ln \left( \frac{D_{gb}}{D_v} \right) \quad (10)$$

where  $R$  is the universal gas constant,  $N_a$  is the Avogadro number,  $T$  is the absolute temperature. Eq. (10) when combined with the Arrhenius representations of the diffusion coefficients can be re-written as

$$\gamma_{gb} = \frac{RT}{2a^2 N_a} \ln \left( \frac{D_{0,gb}}{D_{0,v}} \right) + \frac{1}{2a_0^2 N_a} (Q_v - Q_{gb}) \quad (11)$$

where,  $D_{0,gb}$  and  $D_{0,v}$  are the exponential pre-factors of the grain boundary and bulk diffusivities, respectively.  $Q_{gb}$  and  $Q_v$  are the corresponding activation enthalpies, respectively.

The fundamental concept behind this correlation is that the increased atomic mobility along the GBs is caused by a reduction of the Gibbs free energy of atom-vacancy exchanges at the grain boundary as compared to that in the bulk by an amount equal to the absolute grain boundary energy. This model was further elaborated by Guiraldenq [96], Gupta [97] and Pelleg [98] for various FCC pure metals and binary dilute alloys. Grain boundary energy values estimated for pure Ni using the thermal grooving method [99] and Borisov's approach [92] showed a close agreement, further corroborating this methodology of GB energy estimation. The physics of such a correlation was further developed for FCC [100] and BCC [101] metals and alloys.

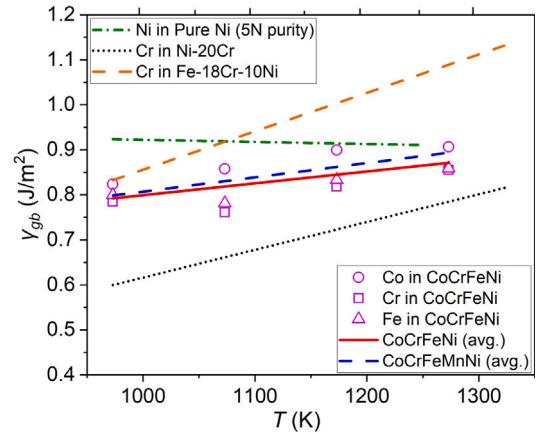


**Fig. 11.** GB energy,  $\gamma_{gb}$ , calculated by Eqs. (10) and (11) for the CoCrFeNi alloy for Co (open circle), Cr (open square) and Fe (open triangle). The solid red line for the CoCrFeNi alloy is the averaged  $\gamma_{gb}$  over the diffusivities of Co, Cr and Fe. These values are compared with unary Ni [92] (green dash-dotted line), binary Ni-20Cr [81] (black dotted line), ternary Fe-18Cr-10Ni [83] (orange dashed line), and quinary CoCrFeMnNi [35] (blue dashed line). (For interpretation of the references to colour in this figure legend, the reader is referred to the web version of this article.)

In this paper, we utilize Eq. (10) to calculate the GB energy ( $\gamma_{gb}$ ) for the CoCrFeNi alloy at the measured temperatures using the data for Co, Cr and Fe. These GB energies are also compared with GB diffusivities in unary (5N purity Ni), binary (Ni-20wt%), ternary (Fe-18wt.%Cr-10wt.%Ni), and quinary CoCrFeMnNi alloys. These comparisons are compiled in Fig. 11.

It can be observed from Fig. 11, that the  $\gamma_{gb}$  values for all the three tracers are relatively similar, which indicates that the Borisov formalism can be used for the CoCrFeNi system. Combining the points for the individual tracers, an averaged temperature dependence has also been plotted in Fig. 11 according to the Eq. (12),

$$\gamma_{gb} = (0.54 \pm 0.10) + (2.64 \pm 0.09) \times 10^{-4} \text{ Jm}^{-2} \quad (12)$$

It can be seen that only for the 5N-purity unary Ni system, the temperature dependence of the GB energy shows the thermodynamically expected negative slope owing to the relatively impurity-free GBs in this system. It was shown previously that in Ni of a lower purity, the slope becomes positive [53,92], similar to the slopes for the alloys in Fig. 11. The  $\gamma_{gb}$  of the CoCrFeNi system is quite similar to that of the quinary CoCeFeMnNi, while the lines for both these alloys lie above the binary Ni-20wt.%Cr and ternary Fe-18wt.%Cr-10wt.%Ni.

## 5. Conclusions

GB diffusion of the constituting elements in CoCrFeNi is measured in the B-type (higher temperatures) as well as C-type (lower temperatures) kinetics diffusion regimes. While a diffusion contribution of only one type of general high-angle GBs is observed at higher temperatures, two distinct branches of the diffusion penetration profiles are resolved at lower temperatures. These two diffusion branches at lower temperature are distinguished as  $D_{gb1}$  (relatively “slow”) and  $D_{gb2}$  (relatively “fast”).

Assuming the product of the segregation factor and the GB width is equal to 0.5 nm, i.e. coincides with the GB width, the triple products determined under the B-type kinetics conditions are found to align perfectly with the “slow” diffusion coefficients following a common Arrhenius-type temperature dependence, corroborating the absence of any strong segregation of the constituting elements at the majority of GBs in CoCrFeNi. A similar behaviour is observed for Mn, too, which is an impurity element in CoCrFeNi.

The origin of an additional short-circuit contribution at the lower temperatures is discussed in terms of induced stresses and accompanying GB-related dislocation networks due to phase decomposition at certain grain boundaries. The density of such grain boundaries in CoCrFeNi is evaluated to be lower than the density of similar GBs in quinary CoCrFeMnNi, as it followed from a comparison of the corresponding penetration profiles. This behaviour is explained by the differences in the thermodynamic driving forces for phase decomposition as well as the rates of atomic diffusion in these two HEAs.

The applicability of the Borisov formalism for the estimation of the grain boundary energy,  $\gamma_{gb}$ , from the diffusivity values is examined for the CoCrFeNi system and reasonable  $\gamma_{gb}$  values are determined.

## Declaration of competing interest

The authors declare that they have no known competing financial interests or personal relationships that could have appeared to influence the work reported in this paper.

## Acknowledgements

Financial support of the German Research Foundation (DFG) via SPP2006, project WI 1899/32-2, and project DI 1419/19-1 is acknowledged. KGP is grateful for the financial support of Max-Planck Gesellschaft through Max-Planck-India partner group. KGP and KG acknowledge the use of National Facility for Atom Probe Tomography (NFAPT) for correlative microscopy studies.

## Appendix A. Supplementary data

Supplementary material related to this article can be found online at <https://doi.org/10.1016/j.actamat.2023.119588>.

## References

- [1] D. Miracle, O. Senkov, A critical review of high entropy alloys and related concepts, *Acta Mater.* 122 (2017) 448–511, <http://dx.doi.org/10.1016/j.actamat.2016.08.081>.
- [2] B.S. Murty, J.W. Yeh, S. Ranganathan, P. Bhattacharjee, *High-Entropy Alloys*, Elsevier, 2019.
- [3] R. Jain, A. Jain, M. Rahul, A. Kumar, M. Dubey, R.K. Sabat, S. Samal, G. Phanikumar, Development of ultrahigh strength novel Co-Cr-Fe-Ni-Zr quasi-peritectic high entropy alloy by an integrated approach using experiment and simulation, *Materialia* 14 (2020) 100896, <http://dx.doi.org/10.1016/j.mtl.2020.100896>.
- [4] U. Sunkari, S. Reddy, B. Rathod, S. Kumar, R. Saha, S. Chatterjee, P. Bhattacharjee, Heterogeneous precipitation mediated heterogeneous nanostructure enhances strength-ductility synergy in severely cryo-rolled and annealed CoCrFeNi<sub>2.1</sub>Nb<sub>0.2</sub> high entropy alloy, *Sci. Rep.* 10 (2020) 1–9, <http://dx.doi.org/10.1038/s41598-020-63038-z>.
- [5] F. Maresca, W. Curtin, Mechanistic origin of high strength in refractory BCC high entropy alloys up to 1900K, *Acta Mater.* 182 (2020) 235–249, <http://dx.doi.org/10.1016/j.actamat.2019.10.015>.
- [6] S. Shuang, Z. Ding, D. Chung, S. Shi, Y. Yang, Corrosion resistant nanostructured eutectic high entropy alloy, *Corros. Sci.* 164 (2020) 108315, <http://dx.doi.org/10.1016/j.corsci.2019.108315>.
- [7] R. Sharma, A. Roy, P.S. De, Equimolar AlCuFeMn: A novel oxidation resistant alloy, *Intermetallics* 135 (2021) 107215, <http://dx.doi.org/10.1016/j.intermet.2021.107215>.
- [8] S. Sun, Y. Tian, H. Lin, H. Yang, X. Dong, Y. Wang, Z. Zhang, Achieving high ductility in the 1.7 GPa grade CoCrFeMnNi high-entropy alloy at 77 K, *Mater. Sci. Eng. A* 740 (2019) 336–341, <http://dx.doi.org/10.1016/j.msea.2018.10.094>.
- [9] N. Shah, M. Rahul, G. Phanikumar, Accelerated design of eutectic high entropy alloys by ICME approach, *Metall. Mater. Trans. A* 52 (2021) 1574–1580, <http://dx.doi.org/10.1007/s11661-021-06218-4>.
- [10] I. Kaur, Y. Mishin, W. Gust, *Fundamentals of Grain and Interphase Boundary Diffusion*, John Wiley, 1995.
- [11] S. Divinski, H. Edelhoff, S. Prokofjev, Diffusion and segregation of silver in copper  $\Sigma$  5 (310) grain boundary, *Phys. Rev. B* 85 (2012) 144104, <http://dx.doi.org/10.1103/PhysRevB.85.144104>.
- [12] S. Divinski, M. Lohmann, C. Herzog, Grain boundary diffusion and linear and non-linear segregation of Ag in Cu, *Interface Sci.* 11 (2003) 21–31, <http://dx.doi.org/10.1023/A:1021522620571>.
- [13] V.A. Esin, Y. Souhar, Solvent grain boundary diffusion in binary solid solutions: a new approach to evaluate solute grain boundary segregation, *Phil. Mag.* 94 (2014) 4066–4079, <http://dx.doi.org/10.1080/14786435.2014.980043>.
- [14] R.J. Nedoushan, M. Farzin, D. Banabic, Simulation of hot forming processes: Using cost effective micro-structural constitutive models, *Int. J. Mech. Sci.* 85 (2014) 196–204, <http://dx.doi.org/10.1016/j.ijmecsci.2014.04.026>.
- [15] M.A. Bhatia, S.N. Mathaudhu, K.N. Solanki, Atomic-scale investigation of creep behavior in nanocrystalline Mg and Mg–Y alloys, *Acta Mater.* 99 (2015) 382–391, <http://dx.doi.org/10.1016/j.actamat.2015.07.068>.
- [16] J. Yeh, S. Chen, S. Lin, J. Gan, T. Chin, T. Shun, C. Tsau, S. Chang, Nanostructured high-entropy alloys with multiple principal elements: novel alloy design concepts and outcomes, *Adv. Eng. Mater.* 6 (2004) 299–303, <http://dx.doi.org/10.1002/adem.200300567>.
- [17] M. Vaidya, S. Trubel, B. Murty, G. Wilde, S. Divinski, Ni tracer diffusion in CoCrFeNi and CoCrFeMnNi high entropy alloys, *J. Alloys Compd.* 688 (2016) 994–1001, <http://dx.doi.org/10.1016/j.jallcom.2016.07.239>.
- [18] M. Vaidya, K. Pradeep, B. Murty, G. Wilde, S. Divinski, Bulk tracer diffusion in CoCrFeNi and CoCrFeMnNi high entropy alloys, *Acta Mater.* 146 (2018) 211–224, <http://dx.doi.org/10.1016/j.actamat.2017.12.052>.
- [19] J. Kottke, M. Laurent-Brocq, A. Fareed, D. Gaertner, L. Perrière, L. Rogal, S.V. Divinski, G. Wilde, Tracer diffusion in the Ni–CoCrFeMn system: Transition from a dilute solid solution to a high entropy alloy, *Scr. Mater.* 159 (2019) 94–98, <http://dx.doi.org/10.1016/j.scriptamat.2018.09.011>.
- [20] J. Kottke, D. Utt, M. Laurent-Brocq, A. Fareed, D. Gaertner, L. Perrière, L. Rogal, A. Stukowski, K. Albe, S. Divinski, Experimental and theoretical study of tracer diffusion in a series of (CoCrFeMn) 100-xnix alloys, *Acta Mater.* 194 (2020) 236–248, <http://dx.doi.org/10.1016/j.actamat.2020.05.037>.
- [21] J. Zhang, G.M. Muralikrishna, A. Asabre, Y. Kalchev, J. Müller, B. Butz, S. Hilke, H. Rösner, G. Laplanche, S.V. Divinski, G. Wilde, Tracer diffusion in the  $\sigma$  phase of the CoCrFeMnNi system, *Acta Mater.* 203 (2021) 116498, <http://dx.doi.org/10.1016/j.actamat.2020.116498>.
- [22] S. Sen, X. Zhang, L. Rogal, G. Wilde, B. Grabowski, S.V. Divinski, ‘Anti-sluggish’ Ti diffusion in HCP high-entropy alloys: Chemical complexity vs. lattice distortions, *Scr. Mater.* 224 (2023) 115117, <http://dx.doi.org/10.1016/j.scriptamat.2022.115117>.
- [23] M. Vaidya, G. Muralikrishna, S. Divinski, B. Murty, Experimental assessment of the thermodynamic factor for diffusion in CoCrFeNi and CoCrFeMnNi high entropy alloys, *Scr. Mater.* 157 (2018) 81–85, <http://dx.doi.org/10.1016/j.scriptamat.2018.07.040>.

- [24] J. Dabrowa, W. Kuczka, G. Cieslak, T. Kulik, M. Danielewski, J. Yeh, Interdiffusion in the FCC-structured Al-Co-Cr-Fe-Ni high entropy alloys: experimental studies and numerical simulations, *J. Alloys Compd.* 674 (2016) 455–462, <http://dx.doi.org/10.1016/j.jallcom.2016.03.046>.
- [25] J. Dabrowa, M. Zajusz, W. Kuczka, G. Cieslak, K. Berent, T. Czeppe, T. Kulik, M. Danielewski, Demystifying the sluggish diffusion effect in high entropy alloys, *J. Alloys Compd.* 783 (2019) 193–207, <http://dx.doi.org/10.1016/j.jallcom.2018.12.300>.
- [26] D. Gaertner, K. Abrahams, J. Kottke, V. Esin, I. Steinbach, G. Wilde, S. Divinski, Concentration-dependent atomic mobilities in FCC CoCrFeMnNi high-entropy alloys, *Acta Mater.* 166 (2019) 357–370, <http://dx.doi.org/10.1016/j.actamat.2018.12.033>.
- [27] A. Dash, A. Paul, S. Sen, S. Divinski, J. Kundin, I. Steinbach, B. Grabowski, X. Zhang, Recent advances in understanding diffusion in multiprincipal element systems, *Annu. Rev. Mater. Res.* 52 (2022) <http://dx.doi.org/10.1146/annurev-matsci-081720-092213>.
- [28] J. Zhang, C. Gadelmeier, S. Sen, R. Wang, X. Zhang, Y. Zhong, U. Glatzel, B. Grabowski, G. Wilde, S. Divinski, Zr diffusion in BCC refractory high entropy alloys: A case of 'non-sluggish' diffusion behavior, *Acta Mater.* 233 (2022) 117970, <http://dx.doi.org/10.1016/j.actamat.2022.117970>.
- [29] S. Reddy, S. Bapari, P.P. Bhattacharjee, A. Chokshi, Superplastic-like flow in a fine-grained equiatomic CoCrFeMnNi high-entropy alloy, *Mater. Res. Lett.* 5 (2017) 408–414, <http://dx.doi.org/10.1080/21663831.2017.1305460>.
- [30] M. Vaidya, A. Anupam, J.V. Bharadwaj, C. Srivastava, B. Murty, Grain growth kinetics in CoCrFeNi and CoCrFeMnNi high entropy alloys processed by spark plasma sintering, *J. Alloys Compd.* 791 (2019) 1114–1121, <http://dx.doi.org/10.1016/j.jallcom.2019.03.341>.
- [31] S. Sen, X. Zhang, L. Rogal, G. Wilde, B. Grabowski, S. Divinski, Does Zn mimic diffusion of Al in the HCP Al-Sc-Hf-Ti-Zr high entropy alloys? *Scr. Mater.* 229 (2023) 115376, <http://dx.doi.org/10.1016/j.scriptamat.2023.115376>.
- [32] M. Vaidya, S. Sen, X. Zhang, L. Frommeyer, L. Rogal, S. Sankaran, B. Grabowski, G. Wilde, S. Divinski, Phenomenon of ultra-fast tracer diffusion of Co in HCP high entropy alloys, *Acta Mater.* 196 (2020) 220–230, <http://dx.doi.org/10.1016/j.actamat.2020.06.025>.
- [33] V. Nadutov, V. Mazanko, S. Makarenko, Tracer diffusion of cobalt in high-entropy alloys AlxFeNiCoCuCr, *Metallofiz. Noveish. Tekhnol.* (2023) <http://dx.doi.org/10.15407/mfint.39.03.0337>.
- [34] M. Vaidya, K. Pradeep, B. Murty, G. Wilde, S. Divinski, Radioactive isotopes reveal a non sluggish kinetics of grain boundary diffusion in high entropy alloys, *Sci. Rep.* 7 (2017) 1–11, <http://dx.doi.org/10.1038/s41598-017-12551-9>.
- [35] M. Glienke, M. Vaidya, K. Gururaj, L. Daum, B. Tas, L. Rogal, K. Pradeep, S. Divinski, G. Wilde, Grain boundary diffusion in CoCrFeMnNi high entropy alloy: kinetic hints towards a phase decomposition, *Acta Mater.* 195 (2020) 304–316, <http://dx.doi.org/10.1016/j.actamat.2020.05.009>.
- [36] A. Seoane, D. Farkas, X. Bai, Molecular dynamics studies of sluggish grain boundary diffusion in equiatomic FeNiCrCoCu high-entropy alloy, *J. Mater. Sci.* 58 (2023) 8845–8861, <http://dx.doi.org/10.1007/s10853-023-08568-3>.
- [37] F. J., Z. W., Simulation of bulk and grain boundary diffusion phenomena in a high entropy CoCrFeMnNi alloy by molecular dynamics, *Phys. Scr.* 98 (2023) 035006, <http://dx.doi.org/10.1088/1402-4896/acb17e>.
- [38] P. Wynblatt, D. Chatain, Modeling grain boundary and surface segregation in multicomponent high-entropy alloys, *Phys. Rev. Mater.* 3 (2019) 054004, <http://dx.doi.org/10.1103/PhysRevMaterials.3.054004>.
- [39] J. Luo, N. Zhou, High-entropy grain boundaries, *Commun. Mater.* 4 (2023) 7, <http://dx.doi.org/10.1038/s43246-023-00335-w>.
- [40] P. Lejček, A. Školáková, Grain boundary configurational entropy: a challenge, *J. Mater. Sci.* 58 (2023) 10043–10057, <http://dx.doi.org/10.1007/s10853-023-08634-w>.
- [41] A. Maldonado, K. Misra, R. Misra, Grain boundary segregation in a high entropy alloy, *Mater. Technol.* 38 (2023) 2221959, <http://dx.doi.org/10.1080/10667857.2023.2221959>.
- [42] G. Laplanche, S. Berglund, C. Reinhart, A. Kostka, F. Fox, E.P. George, Phase stability and kinetics of  $\sigma$ -phase precipitation in CrMnFeCoNi high-entropy alloys, *Acta Mater.* 161 (2018) 338–351, <http://dx.doi.org/10.1016/j.actamat.2018.09.040>.
- [43] I. Basu, K. Pradeep, C. Mießén, L. Barrales-Mora, T. Al-Samman, The role of atomic scale segregation in designing highly ductile magnesium alloys, *Acta Mater.* 116 (2016) 77–94, <http://dx.doi.org/10.1016/j.actamat.2016.06.024>.
- [44] H. Zhang, K.G. Pradeep, S. Mandal, D. Ponge, H. Springer, D. Raabe, Dynamic strain-induced transformation: An atomic scale investigation, *Scr. Mater.* 109 (2015) 23–27, <http://dx.doi.org/10.1016/j.scriptamat.2015.07.010>.
- [45] W. Wang, W. Wang, S. Wang, Y. Tsai, C. Lai, J. Yeh, Effects of Al addition on the microstructure and mechanical property of Al<sub>1</sub>CoCrFeNi high-entropy alloys, *Intermetallics* 26 (2012) 44–51, <http://dx.doi.org/10.1016/j.intermet.2012.03.005>.
- [46] Z. Wang, Q. Wu, W. Zhou, F. He, C. Yu, D. Lin, J. Wang, C. Liu, Quantitative determination of the lattice constant in high entropy alloys, *Scr. Mater.* 162 (2019) 468–471, <http://dx.doi.org/10.1016/j.scriptamat.2018.12.022>.
- [47] E. Huang, H. Chou, K. Tu, W. Hung, T. Lam, C. Tsai, C. Chiang, B. Lin, A. Yeh, S.S.H. Chang, Y. Chang, J. Yang, X. Li, C. Ku, K. An, Y. Chang, Y. Jao, Element effects on high-entropy alloy vacancy and heterogeneous lattice distortion subjected to quasi-equilibrium heating, *Sci. Rep.* 9 (2019) 14788, <http://dx.doi.org/10.1038/s41598-019-51297-4>.
- [48] G. Bracq, M. Laurent-Brocq, L. Perrière, R. Pirès, J. Joubert, I. Guillot, The fcc solid solution stability in the Co-Cr-Fe-Mn-Ni multi-component system, *Acta Mater.* 128 (2017) 327–336, <http://dx.doi.org/10.1016/j.actamat.2017.02.017>.
- [49] F. Otto, A. Dlouhý, K.G. Pradeep, M. Kuběnová, D. Raabe, G. Eggeler, E. George, Decomposition of the single-phase high-entropy alloy CrMnFeCoNi after prolonged anneals at intermediate temperatures, *Acta Mater.* 112 (2016) 40–52, <http://dx.doi.org/10.1016/j.actamat.2016.04.005>.
- [50] L. Harrison, Influence of dislocations on diffusion kinetics in solids with particular reference to the alkali halides, *Trans. Faraday Soc.* 57 (1961) 1191–1199.
- [51] A. Paul, T. Laurila, V. Vuorinen, S. Divinski, Thermodynamics, Diffusion and the Kirkendall Effect in Solids, Springer, 2014, <http://dx.doi.org/10.1007/978-3-319-07461-0>.
- [52] S. Divinski, F. Hisker, Y. Kang, J. Lee, C. Herzig, Ag diffusion and interface segregation in nanocrystalline  $\gamma$ -FeNi alloy with a two-scale microstructure, *Acta Mater.* 52 (2004) 631–645, <http://dx.doi.org/10.1016/j.actamat.2003.09.045>.
- [53] D. Prokoshkina, V. Esin, G. Wilde, S. Divinski, Grain boundary width, energy and self-diffusion in nickel: effect of material purity, *Acta Mater.* 61 (2013) 5188–5197, <http://dx.doi.org/10.1016/j.actamat.2013.05.010>.
- [54] J. Fisher, Calculation of diffusion penetration curves for surface and grain boundary diffusion, *J. Appl. Phys.* 22 (1951) 74–77, <http://dx.doi.org/10.1063/1.1699825>.
- [55] A. Le Claire, The analysis of grain boundary diffusion measurements, *Br. J. Appl. Phys.* 14 (1963) 351, <http://dx.doi.org/10.1088/0508-3443/14/6/317>.
- [56] T. Suzuoka, Exact solutions of two ideal cases in grain boundary diffusion problem and the application to sectioning method, *J. Phys. Soc. Japan* 19 (1964) 839–851, <http://dx.doi.org/10.1143/JPSJ.19.839>.
- [57] D. Gaertner, J. Kottke, Y. Chumlyakov, F. Hergemöller, G. Wilde, S. Divinski, Tracer diffusion in single crystalline CoCrFeNi and CoCrFeMnNi high-entropy alloys: Kinetic hints towards a low-temperature phase instability of the solid-solution? *Scr. Mater.* 187 (2020) 57–62, <http://dx.doi.org/10.1016/j.scriptamat.2020.05.060>.
- [58] Z. Zhang, M. Mao, J. Wang, B. Gludovatz, Z. Zhang, S. Mao, E. George, Q. Yu, R. Ritchie, Nanoscale origins of the damage tolerance of the high-entropy alloy CrMnFeCoNi, *Nature Commun.* 6 (2015) 1–6, <http://dx.doi.org/10.1038/ncomms10143>.
- [59] B. Schuh, F. Mendez-Martin, B. Völker, E. George, H. Clemens, R. Pippan, A. Hohenwarter, Mechanical properties, microstructure and thermal stability of a nanocrystalline CoCrFeMnNi high-entropy alloy after severe plastic deformation, *Acta Mater.* 96 (2015) 258–268, <http://dx.doi.org/10.1016/j.actamat.2015.06.025>.
- [60] J.B.Y. Mishin, Chr. Herzig, W. Gust, Grain boundary diffusion: fundamentals to recent developments, *Int. Mater. Rev.* 42 (1997) 155–178, <http://dx.doi.org/10.1179/imr.1997.42.4.155>.
- [61] S.V. Divinski, B.S. Bokstein, Recent advances and unsolved problems of grain boundary diffusion, in: Grain Boundary Diffusion, Stresses and Segregation, Defect and Diffusion Forum, Vol. 309, Trans Tech Publications Ltd, 2011, pp. 1–8, <http://dx.doi.org/10.4028/www.scientific.net/DDF.309-310.1>.
- [62] G.E.D.L. Beke, I. Gódný, F.J. Kedves, The temperature dependence of grain-boundary diffusion of 65Zn in polycrystalline aluminium, *Phil. Mag. A* 56 (1987) 659–671, <http://dx.doi.org/10.1080/01418618708204479>.
- [63] S.V. Divinski, F. Hisker, Y.S. Kang, J.S. Lee, C. Herzig, 59Fe grain boundary diffusion in nanostructured  $\gamma$ -Fe-Ni. Part I: Radiotracer experiments and Monte-Carlo simulation in the type-A and B kinetic regimes, *Int. J. Mater. Res.* 93 (2002) 256–264, <http://dx.doi.org/10.3139/ijmr-2002-0048>.
- [64] S.V. Divinski, F. Hisker, Y.S. Kang, J.S. Lee, C. Herzig, Tracer diffusion of 63Ni in nano- $\gamma$ -FeNi produced by powder metallurgical method: Systematic investigations in the C, B, and A diffusion regimes, *Interface Sci.* 11 (2003) 67–80, <https://api.semanticscholar.org/CorpusID:137361313>.
- [65] L. Klinger, E. Rabkin, Diffusion along the grain boundaries in crystals with dislocations, *Interface Sci.* 6 (1998) 197–203, <http://dx.doi.org/10.1023/A:1008612202019>.
- [66] S. Divinski, J. Geise, E. Rabkin, C. Herzig, Grain boundary self-diffusion in  $\alpha$ -iron of different purity: effect of dislocation enhanced diffusion, *Z. Metallkunde* 95 (2004) 945–952, <http://dx.doi.org/10.1515/ijmr-2004-0173>.
- [67] S.V. Divinski, J. Ribbe, D. Baither, G. Schmitz, G. Replitz, H. Rösner, K. Sato, Y. Estrin, G. Wilde, Nano- and micro-scale free volume in ultrafine grained Cu–1wt.%Pb alloy deformed by equal channel angular pressing, *Acta Mater.* 57 (2009) 5706–5717, <http://dx.doi.org/10.1016/j.actamat.2009.07.066>.
- [68] F. Cao, Y. Chen, S. Zhao, E. Ma, L. Dai, Grain boundary phase transformation in a CrCoNi complex concentrated alloy, *Acta Mater.* 209 (2021) 116786, <http://dx.doi.org/10.1016/j.actamat.2021.116786>.
- [69] J. Li, Y. Wu, Z. Bai, W. Yu, S. Shen, Nanostructure–property relation of  $\Sigma 5$  grain boundary in HfNbZrTi high-entropy alloy under shear, *J. Mater. Sci.* 58 (2023) 6757–6774, <http://dx.doi.org/10.1007/s10853-023-08443-1>.

- [70] S. Ma, W. Liu, Q. Li, J. Zhang, S. Huang, Y. Xiong, B. Xu, T. Yang, S. Zhao, Mechanism of elemental segregation around extended defects in high-entropy alloys and its effect on mechanical properties, *Acta Mater.* (2023) 119537, <http://dx.doi.org/10.1016/j.actamat.2023.119537>.
- [71] Thermo-calc web page, 2023, <https://thermocalc.com/>.
- [72] J. Andersson, T. Helander, L. Höglund, P. Shi, B. Sundman, Thermo-calc & DICTRA, computational tools for materials science, *CALPHAD* 26 (2002) 273–312, [http://dx.doi.org/10.1016/S0364-5916\(02\)00037-8](http://dx.doi.org/10.1016/S0364-5916(02)00037-8).
- [73] F. Otto, A. Dlouhý, K. Pradeep, M. Kuběnová, D. Raabe, G. Eggeler, E. George, Decomposition of the single-phase high-entropy alloy CrMnFeCoNi after prolonged anneals at intermediate temperatures, *Acta Mater.* 112 (2016) 40–52, <http://dx.doi.org/10.1016/j.actamat.2016.04.005>.
- [74] K. Christofidou, E. Pickering, P. Orsatti, P. Mignanelli, T. Slater, H. Stone, N. Jones, On the influence of Mn on the phase stability of the CrMnFeCoNi high entropy alloys, *Intermetallics* 92 (2018) 84–92, <http://dx.doi.org/10.1016/j.intermet.2017.09.011>.
- [75] L. Li, Z. Li, A.K. da Silva, Z. Peng, H. Zhao, B. Gault, D. Raabe, Segregation-driven grain boundary spinodal decomposition as a pathway for phase nucleation in a high-entropy alloy, *Acta Mater.* 178 (2019) 1–9, <http://dx.doi.org/10.1016/j.actamat.2019.07.052>.
- [76] V. Brik, L. Larikov, V. Falchenko, Self-diffusion in cobalt, *Ukrain. Fiz. Zhurn.* 20 (1975) 397.
- [77] I. Kaur, W. Gust, L. Kozma, Handbook of Grain and Interphase Boundary Diffusion Data, Ziegler Press, Stuttgart, 1989, <https://books.google.de/books?id=IQJLAQAIAAJ>.
- [78] J. Cermak, Grain boundary self-diffusion of 51Cr and 59Fe in austenitic Ni–Fe–Cr alloys, *Mater. Sci. Eng. A* 148 (1991) 279–287, [http://dx.doi.org/10.1016/0921-5093\(91\)90830-G](http://dx.doi.org/10.1016/0921-5093(91)90830-G).
- [79] T. Gheno, F. Jomard, C. Desgranges, L. Martinelli, Grain boundary diffusion of chromium in polycrystalline nickel studied by SIMS, *Materialia* 6 (2019) 100283, <http://dx.doi.org/10.1016/j.mtla.2019.100283>.
- [80] A. Huntz, P. Guiraldenq, M. Aucouturier, P. Lacombe, Relation between diffusion processes of radioactive iron and chromium in iron–chromium alloys with 0 to 15% Cr and their reversible  $\alpha$  to  $\alpha$  plus  $\gamma$  transformation, *Mem. Sci. Rev. Metall.* 66 (1969) 85–104.
- [81] P. Moulin, A. Huntz, P. Lacombe, Influence du carbone sur la diffusion du chrome et du nickel en volume et dans les joints de grains de l’alliage Ni–Cr 80/20, *Acta Metall.* 27 (1979) 1431–1443, [http://dx.doi.org/10.1016/0001-6160\(79\)90165-2](http://dx.doi.org/10.1016/0001-6160(79)90165-2).
- [82] R. Perkins, R. Padgett, N. Tunali, Tracer diffusion of 59 Fe and 51 Cr in Fe-17 Wt Pet Cr-12 Wt Pet Ni austenitic alloy, *Metall. Trans.* 4 (1973) 2535–2540, <http://dx.doi.org/10.1007/BF02644255>.
- [83] D. Juve-Duc, D. Treheux, Influence du soufre sur la diffusion intergranulaire dans la solution solide austénitique Fe–Cr–Ni (18% Cr, 10% Ni), *Acta Metall.* 32 (1984) 2063–2068, [http://dx.doi.org/10.1016/0001-6160\(84\)90185-8](http://dx.doi.org/10.1016/0001-6160(84)90185-8).
- [84] P. Guiraldenq, P. Lacombe, Mesure des coefficients d’autodiffusion intergranulaire du fer en phase  $\gamma$  et comparaison avec l’autodiffusion aux joints de grains du fer  $\alpha$ , *Acta Metall.* 13 (1965) 51–53, [http://dx.doi.org/10.1016/0001-6160\(65\)90030-1](http://dx.doi.org/10.1016/0001-6160(65)90030-1).
- [85] N. Aucouturier, P. Lacombe, Diffusion of radioactive iron in grain boundaries of porous and solid cobalt, *Kobalt* 28 (1965) 111.
- [86] P. Guiraldenq, P. Lacombe, Properties of Grain Boundaries, 4th Colloque de Metallurgie, Saclay (1960), Press Universitaires de France, 1961.
- [87] P. Guiraldenq, P. Poyet, Effect of nickel on volume diffusion and on intercrystalline diffusion in austenitic Fe–Cr–Ni alloys. Changes in grain boundary energy as a function of composition, *Mem. Sci. Rev. Metall.* 70 (1973) 715–723.
- [88] E. Budke, T. Surholt, S. Prokofjev, L. Shvindlerman, C. Herzig, Tracer diffusion of Au and Cu in a series of near  $\Sigma = 5(310)[001]$  symmetrical Cu tilt grain boundaries, *Acta Mater.* 47 (1999) 385–395, [http://dx.doi.org/10.1016/S1359-6454\(98\)00381-4](http://dx.doi.org/10.1016/S1359-6454(98)00381-4).
- [89] C. Minkwitz, C. Herzig, E. Rabkin, W. Gust, The inclination dependence of gold tracer diffusion along a  $\Sigma 3$  twin grain boundary in copper, *Acta Mater.* 47 (1999) 1231–1239, [http://dx.doi.org/10.1016/S1359-6454\(98\)00429-7](http://dx.doi.org/10.1016/S1359-6454(98)00429-7).
- [90] A. Gupta, V. Kulitcki, B.T. Kavakbasi, Y. Buranova, J. Neugebauer, G. Wilde, T. Hickel, S.V. Divinski, Precipitate-induced nonlinearities of diffusion along grain boundaries in Al-based alloys, *Phys. Rev. Mater.* 2 (2018) 073801, <http://dx.doi.org/10.1103/PhysRevMaterials.2.073801>.
- [91] M. Daw, M. Chandross, Sluggish diffusion in random equimolar FCC alloys, *Phys. Rev. Mater.* 5 (2021) 043603.
- [92] S. Divinski, G. Rehlitz, G. Wilde, Grain boundary self-diffusion in polycrystalline nickel of different purity levels, *Acta Mater.* 58 (2010) 386–395, <http://dx.doi.org/10.1016/j.actamat.2009.09.015>.
- [93] T. Surholt, C. Herzig, Grain boundary self-diffusion in Cu polycrystals of different purity, *Acta Mater.* 45 (1997) 3817–3823, [http://dx.doi.org/10.1016/S1359-6454\(97\)00037-2](http://dx.doi.org/10.1016/S1359-6454(97)00037-2).
- [94] Z. Tókei, Z. Erdelyi, C. Girardeaux, A. Rolland, Effect of sulphur content and pre-annealing treatments on nickel grain-boundary diffusion in high-purity copper, *Phil. Mag. A* 80 (2000) 1075–1083, <http://dx.doi.org/10.1080/01418610008212101>.
- [95] V. Borisov, V. Golikov, G. Scherbedinskiy, Relation between diffusion coefficients and grain boundary energy, *Phys. Met. Metall.* 17 (1964) 881–885.
- [96] P. Guiraldenq, Diffusion intergranulaire et energie des joints de grains, *J. Phys. Colloques* 36 (1975) C4–201, <http://dx.doi.org/10.1051/jphyscol:1975420>.
- [97] D. Gupta, Grain-boundary energies and their interaction with Ta solute from self-diffusion in Au and Au-1.2 at.% Ta alloy, *Phil. Mag.* 33 (1976) 189–197, <http://dx.doi.org/10.1080/14786437608221103>.
- [98] J. Pelleg, On the relation between diffusion coefficients and grain boundary energy, *Phil. Mag.* 14 (1966) 595–601, <http://dx.doi.org/10.1080/14786436608211954>.
- [99] P. Haremski, L. Epple, M. Wieler, P. Lupetin, R. Thelen, M.J. Hoffmann, A thermal grooving study of relative grain boundary energies of nickel in polycrystalline Ni and in a Ni/YSZ anode measured by atomic force microscopy, *Acta Mater.* 214 (2021) 116936, <http://dx.doi.org/10.1016/j.actamat.2021.116936>.
- [100] L. Changle, L. Song, V. Levente, Predicting grain boundary energies of complex alloys from ab initio calculations, *Scr. Mater.* 203 (2021) 114118, <http://dx.doi.org/10.1016/j.scriptamat.2021.114118>.
- [101] C. Li, S. Lu, S. Divinski, L. Vitos, Theoretical and experimental grain boundary energies in body-centered cubic metals, *Acta Mater.* 255 (2023) 119074, <http://dx.doi.org/10.1016/j.actamat.2023.119074>.